A high-resolution simulation of the ocean during the POMME experiment: Simulation results and comparison with observations

A. Paci, Guy Caniaux, M. Gavart, Hervé Giordani, Marina Lévy, Louis Prieur, Gilles Reverdin

A high-resolution simulation of the ocean during the POMME experiment: Simulation results and comparison with observations

A. Paci,[1] G. Caniaux,[1] M. Gavart,[2] H. Giordani,[1] M. Lévy,[3] L. Prieur,[4] and G. Reverdin[3]

Received 13 September 2004; revised 1 February 2005; accepted 17 May 2005; published 29 July 2005.

[1] A modeling study of physical processes occurring in an area of the northeast Atlantic (21.33°–15.33°W, 38.00°–45.00°N) that was extensively sampled during the Programme Océan Multidisciplinaire Méso Echelle (POMME) (October 2000–September 2001) is carried out. The model is a mesoscale version of the ocean general circulation model OPA developed at the Laboratoire d'Océanographie Dynamique et de Climatologie in Paris. It is used in a three-dimensional limited area domain with a high-resolution grid (approximately 5 km horizontal spacing, 69 vertical levels) and realistic boundary conditions (initial state, air-sea fluxes, open boundary fluxes, and bottom topography). The objectives of the study are to properly simulate the upper ocean dynamics, particularly mesoscale activity and mixed layer evolution, during a key period (restratification) of the POMME experiment (POMME 1 and POMME 2, from February to May 2001) and to compare model results with oceanographic observations collected during the experiment in order to establish confidence in the model. Some results provided by the high-resolution simulation, in particular features related to mixed layer depth and vertical velocities, are also presented. There is no pronounced north-south mixed layer depth gradient, but strong filament-shaped structures associated with stirring at the periphery of eddies are present. Mixed layer restratification is simulated. It is associated with submesoscale mixed layer depth structures and intense vertical velocity filaments in the upper ocean correlated with the relative vorticity gradient field.

Citation: Paci, A., G. Caniaux, M. Gavart, H. Giordani, M. Lévy, L. Prieur, and G. Reverdin (2005), A high-resolution simulation of the ocean during the POMME experiment: Simulation results and comparison with observations, *J. Geophys. Res.*, *110*, C07S09, doi:10.1029/2004JC002712.

1. Introduction

[2] The large-scale transfer of water from the oceanic mixed layer into the interior of the ocean, called subduction, determines the rate at which the surface water mass properties, strongly conditioned by its contact with the atmosphere, are communicated into the deep ocean. This transfer is a major mechanism for the transmission of information from the surface ocean into the deep ocean, and it is a major problem for general circulation models to properly represent subducted water masses. These subducted water masses remain isolated on a decadal timescale from the influence of the atmosphere, therefore understanding the underlying causes of subduction, and its link with air-sea interactions, is of major importance to quantify the role of the ocean in the climate as a carbon and heat reservoir, and to improve ocean models.

[3] In this context, the Programme Océan Multidisciplinaire Méso Echelle (POMME) investigated a particular area of the northern Atlantic in 2001 [*Mémery et al.*, 2005]. This area, located between the Azores Current and the North Atlantic Current, is known to be a transition zone between relatively deep late winter mixed layers in the north (reaching about 500 m) and relatively shallow mixed layers (100–150 m) in the south [*McCartney and Talley*, 1982; *Paillet*, 1999].

[4] According to these studies, the water to the north is advected into this area by the southern branches of the North Atlantic current, where it experiences a net cooling and buoyancy loss. Part of this water is incorporated into the permanent thermocline and flows southward [*Marshall et al.*, 1993; *Spall et al.*, 2000].

[5] Subduction rates in the POMME area are dominated by the formation and subduction of the light variety of subpolar mode water, a vertically homogeneous water that originates in the warm eastward flow of the North Atlantic Current at latitudes around 50°N [*McCartney and Talley*, 1982]. The subduction takes place in the mixed layer depth transition zone, located climatologically around 42°N

[1]Météo-France/Centre National de Recherches Météorologiques–Groupe d'étude de l'Atmosphère Météorologique (GAME), Toulouse, France.
[2]Service Hydrologique et Océanographique de la Marine/Centre Militaire d'Océanographie/Recherche, Observatoire Midi-Pyrénées, Toulouse, France.
[3]Laboratoire d'Océanographie Dynamique et de Climatologie/Institut Pierre-Simon Laplace, Université Paris VI, Paris, France.
[4]Laboratoire d'Océanographie de Villefranche, Villefranche-sur-Mer, France.

0148-0227/05/2004JC002712

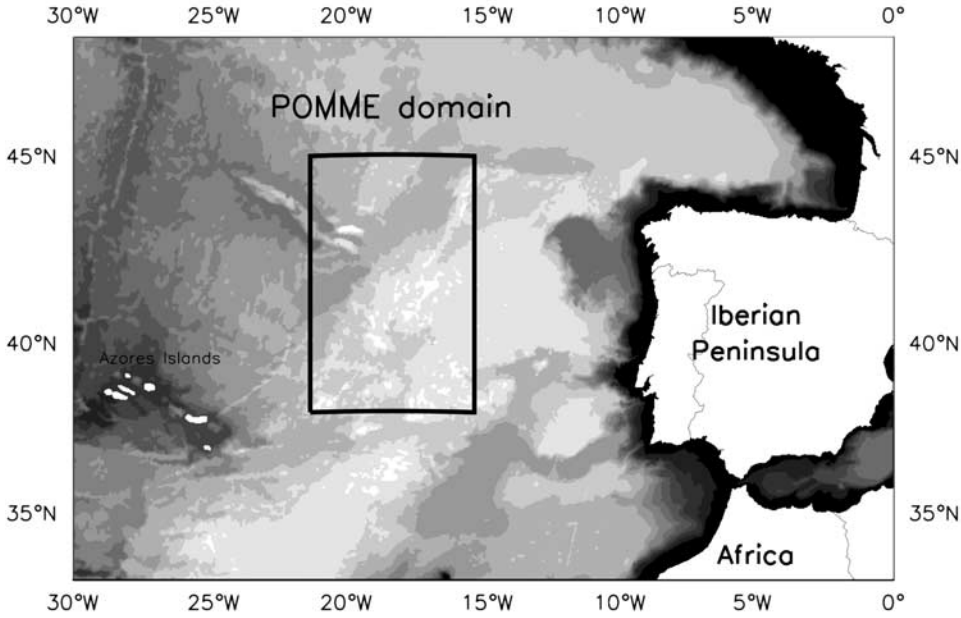

Figure 1. Map of the experiment and simulation domain with geographic names. Bathymetry is represented by 12 shaded isobaths evenly spaced from 5500 m depth to the surface, the lighter tone corresponding to depths greater than 5500 m.

[*Paillet and Arhan*, 1996a, 1996b; *Paillet and Mercier*, 1997; *Paillet*, 1999]. Besides this large-scale view, *Weller et al.* [2004] suggest that mesoscale variability plays an important role in the processes occurring in this area.

[6] POMME was in fact specifically aimed at understanding the role of mesoscale eddies in the subduction mechanisms of 11°–13°C mode water, in biological production and in the carbon budget of the northeast Atlantic; and at describing the fate of organic matter after subduction. The POMME domain consists of a 500 km longitude by 750 km latitude area centered on 41.5°N, 18.3°W (see Figure 1). The field experiment started in the fall 2000 and lasted until the fall 2001. The present study focuses on the restratification period occurring between February 2001 and May 2001, described by two intensive hydrographic surveys, POMME1 and POMME2, hereafter P1 and P2. This period contains the period of effective detrainment as defined by *Qiu and Huang* [1995]. The effective detrainment takes place after late winter when the mixed layer reaches its annual maximum depth and starts to retreat. During this period, water from the mixed layer passes through the depth where the seasonal pycnocline will appear and eventually enters the permanent pycnocline. The amount of detrainment during this period controls the annual mean subduction rate, hence the importance of the period simulated in this study for the POMME project.

[7] P1 was aimed at describing the late winter conditions, in particular the mixed layer depth field and the prebloom distribution of physical and biogeochemical data. Fifty days later, the cruise P2 followed P1 in order to describe the restratification and the spring bloom. Each cruise was divided into two legs (hereafter L1 and L2). The first legs were dedicated to a large-scale survey of the area, whereas the second legs focused on some specific mesoscale structures.

[8] In order to meet the POMME objectives, data isolated in time and space need to be integrated into three-dimensional fields permitting a realistic spatiotemporal representation of the processes occurring in the surface ocean, such as variability induced in the mixed layer by air-sea interactions, or the mesoscale activity. A high-resolution primitive equation oceanic model using measured data is a particularly well adapted tool for this goal. The aim of this study is to properly simulate upper ocean mesoscale physical fields during the mixed layer restratification (occurring from the end of P1L1 to the end of P2L1). A preliminary study has been done by *Caniaux et al.* [2005a, 2005b] where a valuable air-sea fluxes data set covering the POMME domain over one year was produced.

[9] This paper is the first of two, and deals with model results and validations. Indirectly, it also provides valuable insight on the accuracy of the air-sea fluxes, which are a key element determining how well upper ocean mesoscale physical processes are simulated. In the second paper, upper ocean processes will be studied through the calculation of heat and salt budgets, and mixed layer water detrainment and entrainment will be estimated for the period simulated.

[10] The oceanic model is presented in section 2. The initialization procedure and the data used for the boundary conditions are described in section 3. In section 4, the results of the model are presented and its performance is discussed through comparisons with available in situ and objectively analyzed observations in section 5. Some interesting features provided by the simulation regarding mixed layer depth and vertical velocity horizontal scales are presented in section 6. Finally, the main results of this study are summarized in section 7.

2. Regional Ocean Model

2.1. Primitive Equation Ocean Model OPA

[11] The three-dimensional (3-D) model used in this study is derived from the ocean general circulation model

OPA developed at LODYC (Laboratoire d'Océanographie Dynamique et de Climatologie) and described in detail by *Madec et al.* [1999] (available at http://www.ipsl.jussieu.fr). It is a primitive equation (PE) model where the baroclinic and barotropic parts of the horizontal current are treated separately using the rigid lid approximation. The spatial discretization is of second order on an Arakawa C-type grid [*Arakawa*, 1972] and the temporal scheme uses a leap frog method with Asselin smoothing.

[12] The parameterization scheme for the vertical component of turbulent mixing is based on a parameterization of the second-order moments expressed as a function of the turbulent kinetic energy (hereafter TKE), which is given by a prognostic equation. In this formulation, the vertical mixing coefficients are based on the calculation of two turbulent length scales representing upward and downward conversions of TKE into potential energy. This 1.5 turbulence closure model has been developed by *Bougeault and Lacarrère* [1989] for atmospheric cases, adapted by *Gaspar et al.* [1990] for oceanic cases and embedded in OPA by *Blanke and Delecluse* [1993]. Such a scheme was shown to improve the vertical mixing in the tropical Atlantic ocean due to high frequencies in the surface forcing and thereby improved the representation of the vertical mixed layer structure, sea surface temperature and upper layer velocity [*Blanke and Delecluse*, 1993]. The TKE model parameter values used here are those used by *Blanke and Delecluse* [1993], except for the minimum value of the turbulent kinetic energy, $\overline{e}_{\min} = 0.7 \times 10^{-6}$ m^2 s^{-2}, which is the value used in the OPA 8.2 release.

2.2. Regional Version

[13] In the present study, a limited area high-resolution version of the OPA code is used to simulate the ocean in the POMME area between P1 and P2. This mesoscale version was first developed in an initial study using oceanic data collected during the AthenA-88 experiment and realistic atmospheric forcing [*Caniaux et al.*, 1993]. It has been successfully used to study air-sea interaction processes with realistic cases during the SEMAPHORE experiment [*Caniaux and Planton*, 1998] and the TOGA-COARE experiment [*Dourado and Caniaux*, 2001], or coupled with a mesoscale atmospheric model [*Josse et al.*, 1999].

[14] The model domain is a 500 km longitude by 750 km latitude area, extending from 15.33°W to 21.33°W and from 38°N to 45°N, which is the POMME area where the four hydrological surveys were performed. The horizontal regular grid spacing is 1/20°, i.e. about 5 km, allowing us to resolve the third Rossby baroclinic deformation radius (the first, second and third Rossby baroclinic deformation radii calculated from the CTD data at P1 and P2 are about 25 km, 10.5 km and 7.5 km, respectively).

[15] The vertical grid, using prescribed z levels, has 69 levels down to 5650 m with 5-m-thick layers in the first 100 m; the thickness then gradually increasing downward to the bottom. High-resolution bathymetry provided by the Hydrographic Service of the French Navy (SHOM) is used in the model (see Figure 1). The domain is within the abyssal plain of the Iberian basin, with depths of 4500–5000 m. A ridge directed southwest/northeast crosses the zone. In the western part, this ridge contains some seamounts of up to 2000 m and is connected to the Azores Archipelago to the west.

[16] In this configuration the simulation domain includes 121 × 141 horizontal grid points. The high resolution of the model allows us to simulate explicitly mesoscale eddies. This is of particular importance since understanding the effect of mesoscale features on dynamic and biological processes is one of the major objectives of the POMME experiment. Therefore special attention has been paid to the horizontal dissipation of density and momentum. It is included through a biharmonic operator acting along model levels, which is a more scale-selective operator than a second-order (harmonic) operator. The same dissipation coefficient has been taken for tracers (diffusivity) and dynamics (viscosity). The coefficient has been adjusted in order to dissipate the energy that cascades toward the grid scale and thus ensure the stability of the model while not interfering with the solved mesoscale activity. The smallest possible value to avoid numerical noise, $|K| = 1.5 \times 10^9$ m^4 s^{-1}, has been retained.

2.3. Open Lateral Boundaries

[17] One of the main difficulties in modeling a limited area of the ocean is the treatment of the open lateral boundaries. In a PE model, no formulation of boundary conditions is well posed due to the nonhyperbolic system of partial differential equations in the inviscid case [*Sundström and Elvius*, 1979; *Mahadevan and Archer*, 1998]. This problem must be studied in detail and often calls for case-specific solutions. In the present case, many eddies are present in the area, and the boundary runs through some of them. The open boundary condition used here has been formulated by *Gavart et al.* [1999], in order to improve the larger space- and timescales with what was used before in the limited area of the OPA code, i.e., a simple Newtonian relaxation zone [*Caniaux and Planton*, 1998].

[18] The *Gavart et al.* [1999] approach is based on a surrounding recirculation area separated from the physical domain (the interior) by a buffer zone in which T and S fields are damped. The open domain is embedded inside a closed domain and separated from it by a sponge zone. The waves are damped across the boundary because they are indirectly forced by the damping on T and S fields, therefore no action on the velocity field is needed. The latter is only constrained by the geostrophic balance inside the sponge layer. This technique has proven to be very efficient for small extent open domains crossed by energetic features like jets or meddies as in the Azores region [*Gavart et al.*, 1999], and it allows us to perform a simulation on a longer period of time than that of *Caniaux and Planton* [1998]. The larger the damping area, the more the dynamics of the interior domain are perturbed. The smaller the damping area, the more the control of mesoscale structures present near the boundaries is difficult. Therefore it is necessary to reach a compromise in order to obtain the best possible simulation. The surrounding recirculation area is six grid points wide. The damping area, includ-

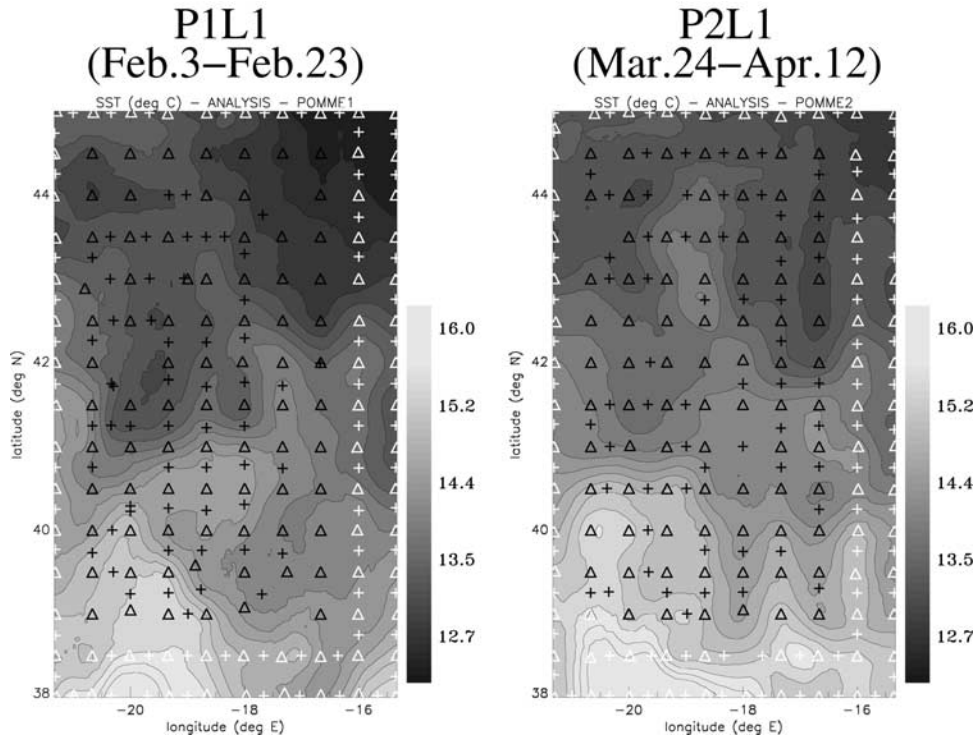

Figure 2. Hydrological surveys performed during the first leg of POMME 1 and POMME 2, with the conductivity-temperature-depth (CTD) shots by the R/V *L'Atalante* (black triangles) and R/V *D'Entrecasteaux* (white triangles), expandable bathythermograph (XBT) shots by the R/V *L'Atalante* (black crosses) and R/V *D'Entrecasteaux* (white crosses), and sea surface temperature from the objective analyses performed on these data sets.

ing the recirculation area, is 12 grid points wide. The way T and S restoring fields are obtained is described in the following section.

3. Initialization and Boundary Conditions

3.1. POMME 1 and Initial Fields

3.1.1. Initial Mass Fields

[19] During P1L1 (3–23 February 2001), the R/V *D'Entrecasteaux* and the R/V *Atalante* performed a joint hydrographic survey covering the POMME domain (see Figure 1), including conductivity-temperature-depth (CTD) measurements every 50 km and an expendable bathythermograph (XBT) measurement between each CTD on the R/V transects. The survey was covered in 20 days, and an impressive amount of data, 145 CTD and 111 XBT were collected, resulting in extensive coverage of the main mesoscale features.

[20] In using this data, special care has been taken in order to provide the best estimates for both the temperature and salinity fields at each level of the model. First we reconstruct salinity from XBT temperature measurements in the zone where we were able to build a reliable temperature-salinity relation from the CTD measurements, i.e., between 600 m and the 16°C isotherm (North Atlantic Central Water (NACW)). Indeed, the NACW is characterized by a tight relationship between T and S [*Arhan*, 1990]. Note that only XBT temperature data from which it was possible to calculate salinity was kept, in order to produce an homogeneous data set in temperature and salinity. This data has been vertically interpolated onto the 69 vertical levels of the model and objectively analyzed onto the horizontal grid for all vertical levels. The objective analysis procedure used has been done in two steps as by *Caniaux and Planton* [1998]. The annual climatological fields from the Levitus World Ocean Atlas 1994 [*Levitus and Boyer*, 1994] has been corrected with the mean bias relative to our data set at each vertical level. This corrected climatology has been considered as the first guess for a time-dependent analysis using our T and S data set. This guess has been used to give spatial coherence to the analyzed fields, i.e., to avoid the patchiness that would have resulted from space-scale differences between the data (50–25 km) and analysis (5 km) grids if a first guess had not been used. Then at each model grid point, the climatology has been corrected using observations which lie within one influence time/space radius around the grid point, following the procedure of *De Mey and Menard* [1989]. An isotropic space correlation radius of 50 km, consistent with mesoscale structure dimensions, and a decay e-folding time of 10 days, in order to time center the analysis on the midsurvey date, have been used. This analysis, centered on 13 February, is the model initial state.

[21] The analyzed SST field is shown in Figure 2. The main feature is a front located around 41°N that separates cold water in the north from warmer and saltier (not shown) water in the south. The domain-averaged SST and SSS, respectively 13.94°C and 35.848 are very close to their February climatological counterparts, 13.85°C and

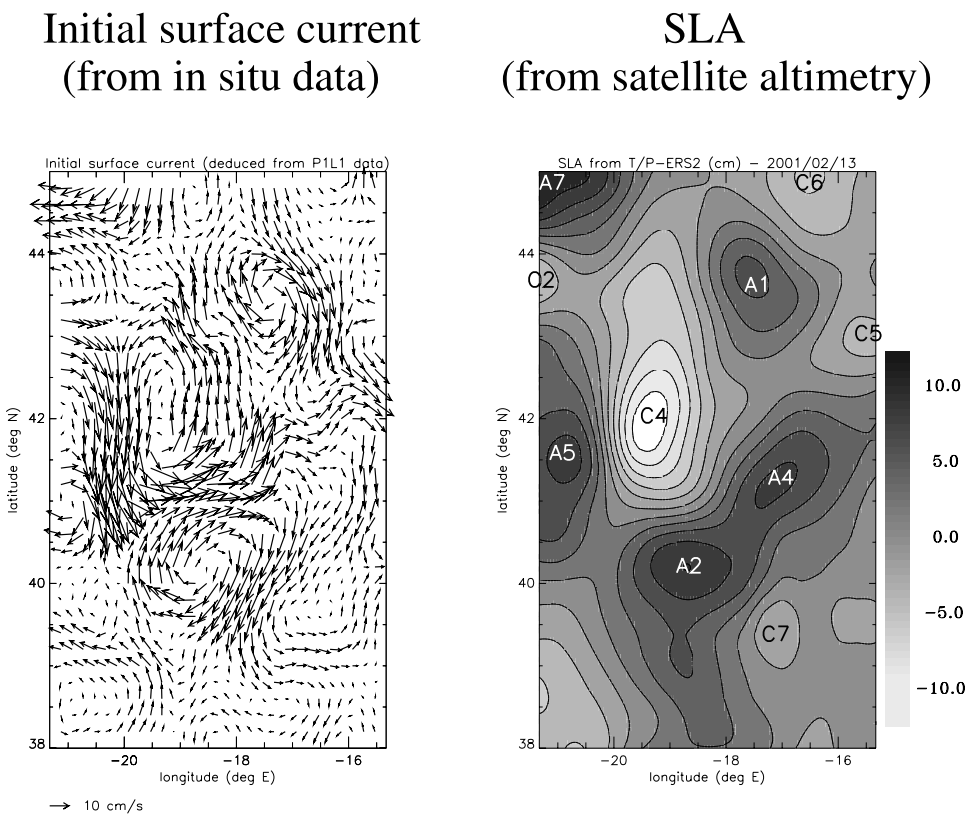

Figure 3. Synoptic charts of the initial current (P1L1 midsurvey on 13 February 2001) and sea level anomalies (SLA) at the same stage. Initial currents are deduced through geostrophy from the analysis of P1L1 hydrological survey using a reference level at about 1700 m. Sea level anomalies are obtained from merged TOPEX/Poseidon and ERS-2 data. Note that the average circulation in the area is much smaller than the eddy structure velocities [*Reverdin et al.*, 2005].

35.827, respectively [*Stephens et al.*, 2002; *Boyer et al.*, 2002].

3.1.2. Initial Currents

[22] The initial mass field analysis has been used to initialize the current field through the geostrophic approximation using a reference level of no motion, as done by *Caniaux and Planton* [1998]. The level 54 (about 1700 m) has been chosen because it gives the best results when we compare initial state and simulated currents with vessel-mounted acoustic Doppler current profiler (VMADCP) observed currents (see section 5.2). It is also the deepest level above bottom topography, and it is close to the reference level estimated by *Stramma* [1984] for the region considered here. This reference level of no motion is only used at this stage. The initial current is also the only feature of the simulation that depends on this level. The resulting surface currents deduced from the P1L1 mass field analysis are presented and compared with sea level anomalies deduced from satellite data in Figure 3. The correlation between these currents and the sea level anomalies is notable, considering that the two data sets are independent. The circulation is marked by a zonal jet about 50 km wide crossing the domain around 41°N, with peak velocities of up to 30 cm s^{-1}. This current forms two cyclonic meanders around 20°W and 17°W, and has clear signatures in thermosalinograph data (see section 5.1). Figure 3 shows also many cyclonic (C2, C4, C5, C6 and C7) and anticyclonic (A1, A2, A4, A5, A7) eddies observed during P1 and P2, which were much more numerous than previously reported by *Paillet* [1999] (the mesoscale eddy nomenclature is presented by *Mémery et al.* [2005]).

[23] The presence of the mesoscale eddies identified during P1 in the initial velocity field confirm the good quality of the mass field analysis. The most important structures for the upper ocean dynamics in the POMME domain between P1 and P2 are A1, A2 and C4. Hydrographic measurements show that A2 and C4 are associated with warm and cold anomalies respectively. C4 has been observed over more than 6 months and A1 over a full year during the POMME experiment [*Assenbaum and Reverdin*, 2005]. The strongest part of the jet is located between A2 and C4, at approximately 41°N. Note that the deepest mixed layer area during the POMME experiment was observed in A7, located in the northwestern corner of Figure 3.

3.2. Lateral Boundaries

[24] Owing to the strong mixed layer evolution (restratification period) during the period simulated in the present experiment, T and S restoring fields need to evolve in time. Because of the lack of large-scale information during the simulation, or accurate values from a coarser mesh grid outer model, these fields are simply linearly interpolated

between the initial time step value from the P1L1 hydrographic survey and the value derived from the P2L1 survey made at the end of the restratification period.

[25] Therefore a second analysis (see Figure 2), used to compute the T and S restoring fields in the sponge layer, has been done using the 145 CTD and 117 XBT provided by P2L1 (24 March–12 April) and the method explained above. This analysis, centered on 3 April, will also provide a means for the verification of model forecasts at the same stage (see section 5.4).

[26] The damping fields are thus the temperature and salinity fields linearly interpolated in time between the P1L1 analysis (13 February) and the P2L1 analysis (3 April). They are kept constant, equal to the P2L1 analysis values, from 4 April to the end of the simulation (20 May). This procedure is used to approximate the changes in the characteristics of large-scale water masses at the lateral boundaries, as explained above. The information used for restoring T and S at the boundaries comes from the CTD and XBT located at the POMME domain boundaries. As the damping area is excluded from the model validations presented in section 5, this data will not be used for the comparison with observations.

3.3. Surface Forcing

[27] Air-sea fluxes are computed through a method validated by comparison with in situ measurements at various locations and seasons, using data from the SEMAPHORE, CATCH, FETCH, EQUALANT99 and POMME campaigns [*Weill et al.*, 2003]. Further validation of the method has been done during the POMME experiment [*Caniaux et al.*, 2005a].

[28] Different data sets are used to estimate the fluxes. Hourly surface irradiances (solar and downward longwave radiative fluxes) are derived from the geostationary METEOSAT satellite data set collected by the Centre de Météorologie Spatiale (Meteo-France, Lannion), following the method developed by *Brisson et al.* [1994], and validated through comparison with in situ measurements carried out by *Eymard et al.* [1996].

[29] The shortwave irradiance was then corrected using an albedo of 0.06, which is consistent with a wide range of weather conditions at sea [*Payne*, 1972]. The net longwave radiative flux at the sea surface was obtained by subtracting the upward flux, computed with analyzed sea surface temperature (using satellite and in situ data as explained below), from the satellite downward radiation, assuming an emissivity of the sea surface of 0.97 and a longwave reflectance of 0.045 [*Mikhaylov and Zolotarev*, 1970]. Shortwave (solar) irradiance fields are sampled on a 0.04° grid and longwave (infrared) irradiance on a 0.08° grid. These fluxes have been averaged on a 5-km-radius circular area around each model grid point.

[30] The turbulent heat fluxes and wind stress are computed using classical bulk formulae for the upward sensible and latent heat flux:

$$H_s = \rho_a Cp C_h |\mathbf{V}|(\mathrm{SST} - T_a), \quad (1)$$

$$L_E = \rho_a Lv C_e |\mathbf{V}|(q_s - q_a), \quad (2)$$

and, for the flux of horizontal momentum,

$$\tau = \rho_a C_d |\mathbf{V}|\mathbf{V}. \quad (3)$$

In these expressions, ρ_a is the air density, Lv the latent specific heat, q_s the surface specific humidity, SST is the sea surface temperature, $\mathbf{V}$ the wind speed vector, T_a and q_a the air temperature and humidity respectively. The surface forcing fluxes are calculated using analyses obtained from observed SST rather than using model SST. This method has been chosen in order to reduce the model drift. The SST fields consist of in situ SST from over a hundred drifters and floats, one mooring, and several ships, which were assimilated by optimal interpolation in a first guess based on Advanced Very High Resolution Radiometer (AVHRR) satellite-derived SST [*Caniaux et al.*, 2005a]. These daily fields are calculated on a 5 km resolution grid. The meteorological fields T_a, q_a, pressure for computation of ρ_a, $\mathbf{V}$, and precipitation rates, are derived from operational analyses from the European Centre for Medium-Range Weather Forecasts (ECMWF) model. They are available every six hours on a 30 km grid. These fields have been space-interpolated on the model grid. The coefficients C_h, C_e, C_d are calculated using ship measurements of turbulent fluxes [*Caniaux et al.*, 2005a].

[31] The fluxes obtained are corrected using an optimization method based on a one dimensional oceanic model forced by lateral advection terms reconstructed from data, in order to equilibrate the annual mixed layer heat content deduced from the POMME data set [*Caniaux et al.*, 2005b]. Then, the daily fluxes produced are time interpolated at each time step of the model. The resulting domain-averaged net heat flux and wind stress are represented in Figure 4. The two fields are characterized by large day-to-day variations. P1L1 is the end of the cooling period, with time-averaged net heat fluxes still being negative (about -30 W m^{-2}). From P1L2 (28 February–19 March) to P2L2 (17 April–3 May) the upper ocean is warmed by air-sea fluxes: the time-averaged net heat flux is about 50 W m^{-2}, with a value of 76 W m^{-2} over P2L1, the period of maximum warming. This warming is dominated by the solar flux; latent and sensible heat fluxes remaining comparatively small. On the one hand, this warming period is reinforced by a few anticyclonic periods of low winds favorable to restratification, as will be shown in section 4.4. On the other hand, some large wind stress episodes may temporarily interrupt the restratification process, and produce vertical mixing.

[32] The time-averaged net heat flux over the simulated period is also presented in Figure 4. The high-resolution air-sea fluxes obtained contain mesoscale features. These features seen in Figure 4 are the fingerprint of oceanic mesoscale eddies. In particular cyclonic cold-core eddies are associated with larger net heat fluxes [*Bourras et al.*, 2004].

4. Simulation Results

4.1. Surface and 200 m Temperature

[33] Model surface and 200 m temperature outputs at P1L1 (day 49 of year 2001, hereafter day 49, 18 February), P1L2 (day 68, 9 March), P2L1 (day 93, 3 April) and P2L2 (day 116, 26 April) are shown in Figure 5.

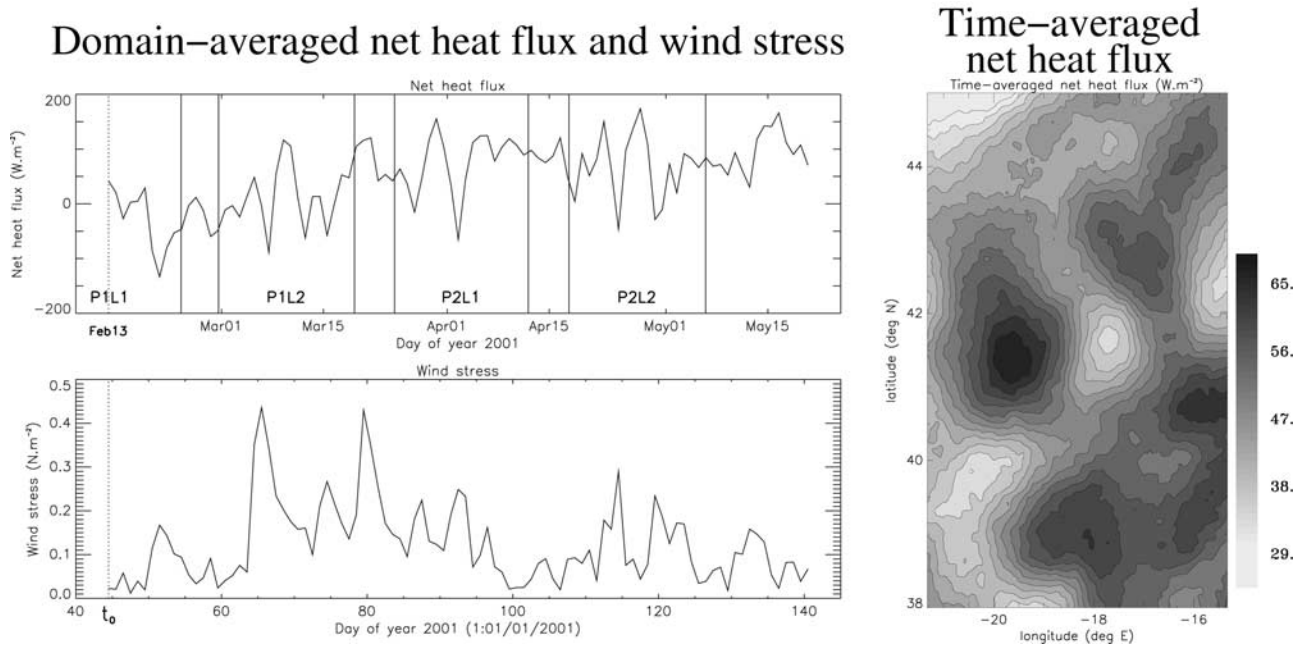

Figure 4. Atmospheric forcings. (left) Temporal evolution of the domain-averaged atmospheric forcing. Net heat flux (sum of shortwave, longwave, latent heat, and sensible heat) and wind stress are presented in W m^{-2} and N m^{-2}, respectively. At P1L2 the upper ocean enters a warming period favorable for restratification, which is reinforced by a few anticyclonic periods, but some wind maxima may interrupt it temporarily. (right) Time-averaged net heat flux over the simulated period.

[34] One of the main features of the simulation is the warming of upper ocean waters, in response to positive net surface heat fluxes associated with quite weak winds as noted earlier in section 3.3. On average, over the whole simulation domain, the surface temperature rises between 13 February (middle of P1L1) and 12 April (end of P2L1) by about 0.8°C, and the southwest warmer water temperature rises by almost 1°C between P2L1 and P2L2, in good agreement with SST analysis using satellite and in situ data [*Caniaux et al.*, 2005a].

[35] Besides this domain-scale evolution, the most striking feature is the strong deformation of the fields by advection and stirring induced by mesoscale eddies. At the beginning of the simulation the SST front located near 41°N, 19°W has a mean temperature gradient of about 2°C over 100 km (see P1L1 SST snapshot in Figure 5). The front separates cold waters between 12.2°C and 13.2°C in the north from warm (and salty, not shown) waters between 15.0°C and 16.0°C in the south. The overall direction of the front is east-west, and its shape develops two warm tongues toward the north: the first one near 42°N, 17.5°W, close to the center of the area, and the second one more to the west, near 42°N, 21°W. The cold-core (SST of about 13.5°C) cyclonic eddy C4 centered around 42°N, 19.5°W is located between these two warm crests. The strongest part of the front, where the surface temperature gradient reaches 3.5°C over 100 km, is located between C4 and the warm-core (SST of about 15.5°C) anticyclonic eddy A2 centered around 40°N, 18.5°W.

[36] Between P1L1 and P2L1 (50 days later), the first warm crest became stronger and extended further to the north reaching 43°N 18°W (see P1L2 and P2L1 T(200 m) snapshots in Figure 5). In the meantime, cold water from the northeast, near 44.5°N, 16°W, was advected southward, toward 43°N, 17°W. These warm and cold waters (T of respectively about 14.0°C and 12.5°C at 200 m) are partly entrained by the anticyclonic eddy called A1 centered around 43°N, 18°W, where they are mixed together.

[37] The 200 m temperature fields are very coherent with surface temperature fields up to P2L1. In particular the front near 41°N is very coherent in the vertical during P1L1 and P1L2. From P2L1 differences between surface and 200 m fields are increasing as a consequence of the upper ocean warming.

[38] Note that fields on day 49 (18 February) contain significantly less high-resolution features than the others; indeed the initial state does not contain information at the model grid scale (5 km) and the model needs about 10 days to generate the missing scales, as it will be shown in section 6.2.

4.2. Sea Level Anomalies and Horizontal Currents

[39] Model sea level anomalies (hereafter SLA) and horizontal currents in the 60–460 m layer at P1L1 (18 February), P1L2 (9 March), P2L1 (3 April) and P2L2 (26 April) are shown in Figure 5.

[40] Mesoscale eddies A1, A2 and C4 are annotated on the plot of SLA. A2 moves southwestward during the simulated period, whereas the position of C4 does not really change. A1 moves along a small circle in the clockwise direction. In fact, A1 has been observed over a full year from September 2000 to September 2001. After drifting southwestward through March 2001, it remained in the same part of the domain until the end of the experiment

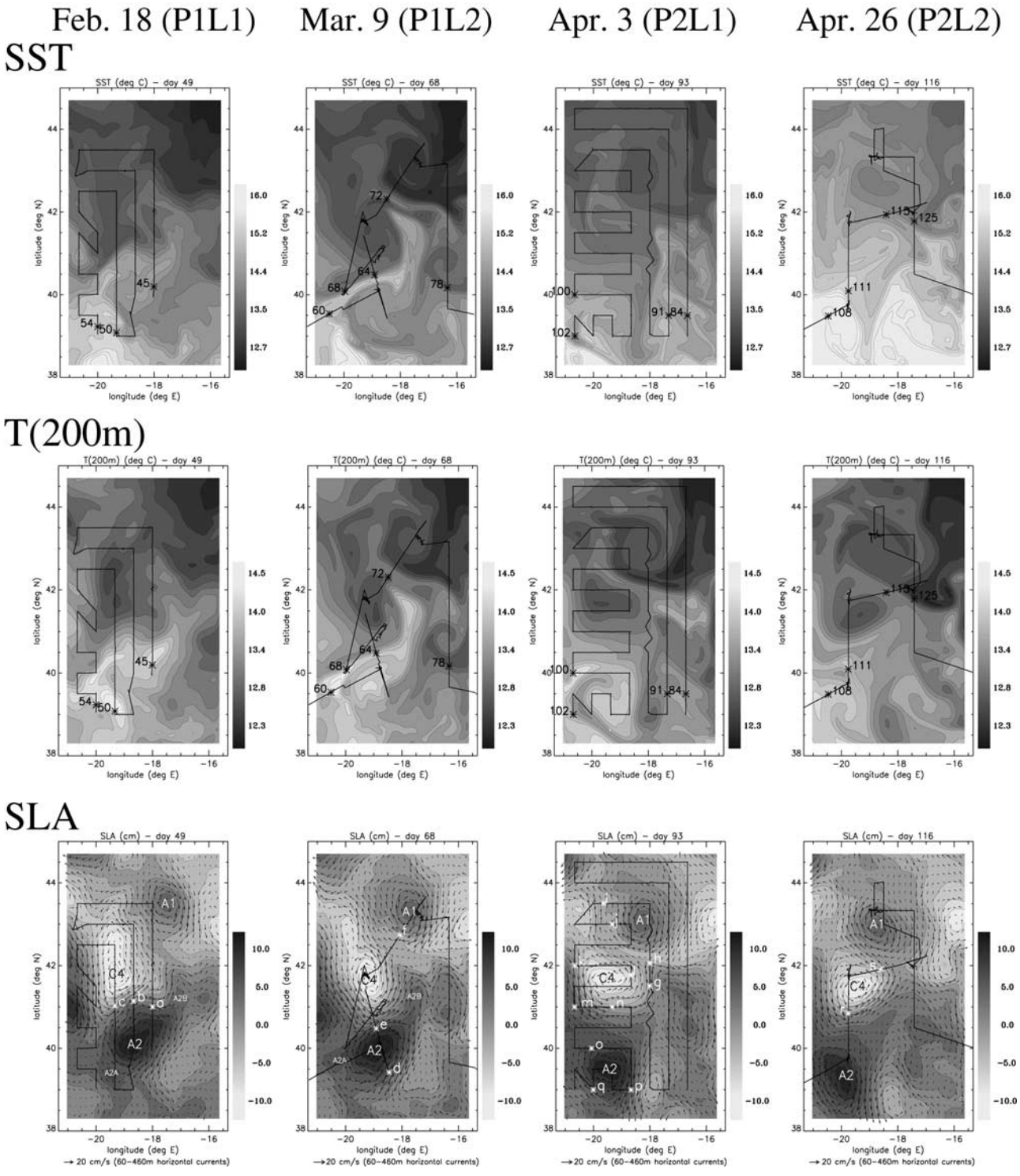

Figure 5. Synoptic charts of simulated sea surface temperature (SST), 200 m temperature, and SLA a few days after the beginning of the simulation during P1L1 and in the middle of P1L2, P2L1, and P2L2. Horizontal currents in the layer 60–460 m and position of the mesoscale eddies A1, A2, and C4 are superimposed on SLA. Black lines are the cruise route during each period, black numbers are related to thermosalinograph (TSG) and conductivity-temperature-depth (CTD) data analysis (section 5.1), and white letters are related to vessel-mounted acoustic Doppler current profiler (VMADCP) data analysis (section 5.2).

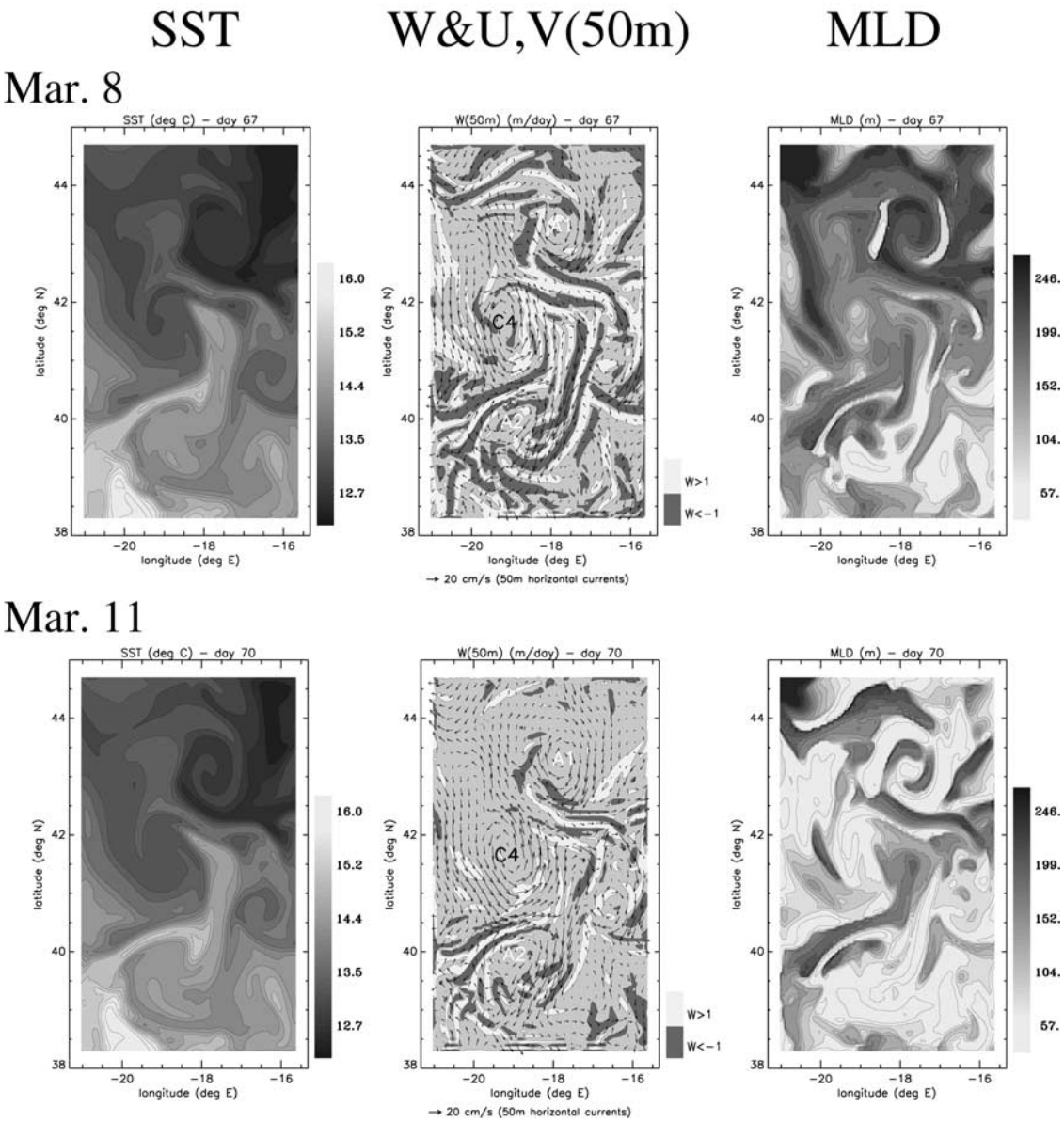

Figure 6. One day averaged SST, vertical and horizontal velocities at 50 m depth, and mixed layer depth on days 67 and 70 (8 and 11 March) during the mixed layer shallowing (P1L2). The mesoscale eddies seen on temperature and horizontal velocity fields are surrounded by mixed layer and vertical velocities submesoscale structures.

in September 2001 [*Assenbaum and Reverdin*, 2005]. Two small deformations of A2: A2A and A2B, are also annotated on the plot of SLA. Their dimensions are about 50 km (about 10 grid points). They could be related to A2 being unstable to a disturbance with an azimuthal wave number $m = 2$. In P1L1 SLA and T(200 m) snapshots, A2A appears as a small warm-core anticyclonic eddy. A2A clearly interacts with A2 during the simulated period, it rotates in the clockwise direction around A2, as seen when P1L1 and P1L2 snapshots are compared in Figure 5. A small tongue of water from A2A can be seen around the perimeter of A2 in the P1L2 T(200 m) snapshot. Such a feature has been observed in the laboratory experiments of *Griffiths and Hopfinger* [1987], and in the Tasman Sea [*Cresswell*, 1982; *Cresswell and Legeckis*, 1986], just before eddies coalesce.

[41] At P1L1 and P1L2, the SST front (41°N, 19°W) between C4 and A2 is associated with a horizontal current maximum, reaching 36 cm s^{-1}. At P2L1 and P2L2, the distance between C4 and A2 is greater than at P1, and the horizontal current maximum barely reaches 24 cm s^{-1} on the southeastern side of C4. At P2L2, when C4 is closer to A1, there is some horizontal current exchange between the two eddies. Note that between P1 and P2, the northward current on the east side of C4 advects warm water (T of about 14°C at 200 m) to the north and the southward current on the east side of A1 advects cold (and less salty, not shown) water to the south (T of about 12.5°C at 200 m).

4.3. Vertical Velocities

[42] Vertical velocities at 50 m depth as well as horizontal velocities at 50 m depth and SST are shown in Figure 6 on

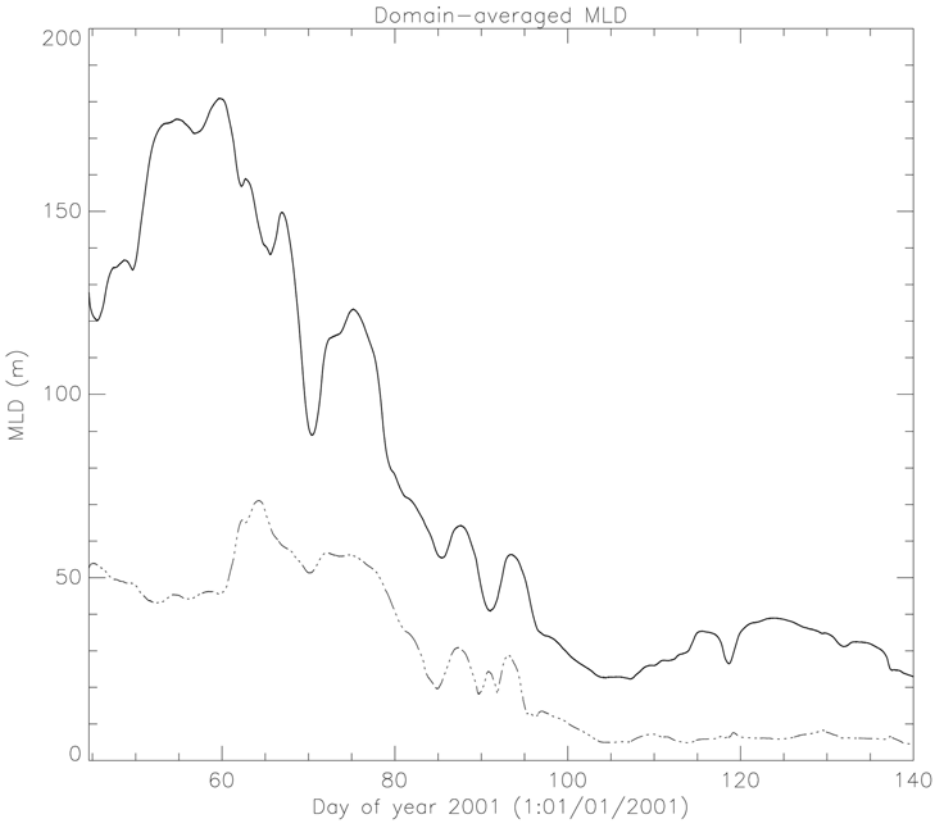

Figure 7. Temporal evolution of the domain-averaged (solid line) and standard deviation (dashed line) of the mixed layer depth.

day 67 (8 March) and on day 70 (11 March). The vertical velocities take the form of filaments correlated with SST fields. Some dipole structures are persistent between day 67 and day 70 near 41°N, 19°W and near 42.5°N, 17°W. These structures are localized at the periphery of the eddies, in particular in the frontal structures extending between eddies, between A2 and C4, and south of A1 respectively. One other striking feature is the change in modeled vertical velocities between day 67 and day 70 in Figure 6, while there is no noticeable change in the oceanic structures. In fact, there are two sources of vertical velocity: the first one is linked to surface fluxes and the second one is linked to internal sources, in particular oceanic structures. The mixed layer depth also plays an important role, determining the range of depths over which the fluxes act. Work is in progress on this subject, and an article is in preparation (H. Giordani et al., manuscript in preparation, 2005).

[43] Vertical velocities are less than 5 m/day, which is smaller than estimates from earlier mesoscale flow studies (40 m/day estimated by *Pollard and Regier* [1992]), but consistent with the quite low eddy kinetic energy (less than 100 cm^2 s^{-2}) associated with the slow evolution of the simulated horizontal geostrophic currents [*Lévy et al.*, 2005] as well as the horizontal geostrophic currents analyzed from satellite altimeter data (S. Giraud, personal communication, 2004). Furthermore, simulated vertical velocity structures have a shape similar to those of the academic study of *Lévy et al.* [2001], and to those present in the simulation of *Giordani et al.* [2005b] in a different three-dimensional model. Estimates from drifters are still in progress and may provide some interesting information about this poorly documented field.

4.4. Mixed Layer Depth

[44] Various mixed layer depth (hereafter MLD) definitions were used by the scientists involved in POMME. The threshold method using a potential density finite difference criterion has been retained as the most suitable one. This method is more stable than the others, as has already been noted by *Brainerd and Gregg* [1995], and stability is of primary importance for the mixed layer budget calculations presented in a forthcoming paper (A. Paci et al., manuscript in preparation, 2005). The reference depth is set at the third z level (12.5 m) to limit diurnal cycle effects, and the density threshold is 0.023 kg m^{-3}, close to the values found in the recent extensive study of *de Boyer Montégut et al.* [2004].

[45] The domain-averaged MLD (hereafter da-MLD) is presented in Figure 7. From the beginning up to day 60 (1 March, end of P1L1), da-MLD increases in depth, as it is the end of the cooling period, and reaches a maximum value of 180 m on day 60. From day 60 to day 100 (1 March–10 April, P1L2 and P2L1), da-MLD rapidly decreases in depth as a whole, with some intermissions during the periods of large wind stress noticed in section 3.3. This period will be referred to as the restratification period. After this period, da-MLD does not change much, except for a slight temporary increase in depth in response to wind stress

maxima on days 114 (24 April) and 123 (3 May) (see Figure 4). At the end of the simulation, the da-MLD is close to 20 m. If the simulation is continued after day 140 (20 May), da-MLD remains close to 20 m until the Fall of 2001, as in other simulations using a 1-D model [*Caniaux et al.*, 2005b], or a simplified 3-D model assimilating geostrophic currents [*Giordani et al.*, 2005a, 2005b], therefore after day 140 the restratification period has ended in the POMME domain. The MLD standard deviation is also shown in Figure 7, and demonstrates that the absolute variation of MLD in the POMME domain is smaller after the restratification period than before.

[46] As expected, there are deeper mixed layers in the north (up to nearly 400 m in the northwest corner) than in the south (less than 50 m in some area) at the beginning of the simulation (not shown). However, the gradient is much weaker than what is usually seen in numerical model predictions [e.g., *Williams et al.*, 1995; *Valdivieso da Costa et al.*, 2005]. Moreover, the MLD field is far from amounting to a simple south-north gradient. Indeed, the MLD is filament shaped and some filaments are persistent during the restratification, particularly at fronts between eddies as seen in Figure 6 (day 67 and day 70, 8 and 11 March) for example for the front located near 41°N (between A2 and C4), and for the front located south of A1. These structures are correlated with SST and vertical velocity structures and seem to result from the interplay between the atmospheric forcing and the deformation induced by mesoscale eddies. A persistent deeper mixed layer area located in the northwest corner is clearly visible in Figure 6. This area is present over the whole simulation, in accordance with in situ observations (a 400 m MLD was deduced from one of the CTD gathered during P2L1), and corresponds to the strong anticyclonic eddy A7 which partly intersects the domain. To conclude, restratification appears to be a process neither temporally nor spatially uniform, as is usually found in lower-resolution studies. Finally, it is important to note that very similar submesoscale vertical velocities and MLD structures were also present in the simulation of *Giordani et al.* [2005b] in a different three-dimensional model.

5. Model-Data Comparisons

5.1. Thermosalinograph and Conductivity-Temperature-Depth Data

[47] Time series of observed and simulated sea surface and subsurface temperature and salinity along the ship track during P1L1, P1L2, P2L1 and P2L2 are shown in Figure 8. Sea surface data are obtained from 15 min averaged *Atalante* thermosalinograph (TSG) data, whereas 200 m data are obtained from the CTD collected during the surveys. Simulated fields at data time are interpolated at data position. There is no significant bias between observed and modeled fields, except during P2L2. P2L2 was largely composed of four long CTD stations, so that T and S evolution is more a temporal variation than a spatial variation and small errors in the localization of modeled thermohaline structures result in the large discrepancies seen in Figure 8. In fact, around two thirds of the time during P2L2, model and data fields are compared at a location that does not evolve with time, while during most of the time during P1L1 and P2L1 the ship is moving across mesoscale structures. Therefore during P1L1 and P2L1 a small error in the localization of a modeled structure appears during a very short time in Figure 8 and naturally disappears into the general pattern. Model ability to properly reproduce temperature and salinity mesoscale structures is excellent over the whole period simulated, as attested by the correlation coefficients (respectively 0.92 and 0.87 for surface temperature and salinity, 0.89 and 0.88 for 200 m temperature and salinity).

[48] Furthermore, Figure 8 illustrates many peaks from mesoscale structures. The most interesting of them are pointed out by vertical dashed lines and corresponding ship positions are indicated by black asterisks in Figure 5. Each peak is identified by the same number (2001 day number) in Figure 5 and in Figure 8. At the beginning of the simulation (day 45), the ship is close to the center of the warm-core eddy A2 (see P1L1 snapshots in Figure 5), therefore surface and 200 m temperature decrease quickly as the ship moves northward and crosses the front located between A2 and C4. The ship also crosses this front during P1L2, on day 64. At this time the surface front had a temperature gradient of about 2°C over 100 km and a salinity gradient of about 0.35 over 100 km. Also, at the end of P2L1, on day 102, the ship crosses the perimeter of A2; and at the beginning of P2L2, on day 108, the ship enters the area through A2.

[49] The two other peaks (days 50 and 54) in the P1L1 period occur when the ship crosses the front and then the small warm-core eddy A2A (see SLA snapshot at P1L1 in Figure 5, also visible in SSS (not shown)).

[50] The peak on day 68 occurs when the ship crosses the small tongue of water from A2A winding round A2. Three other peaks correspond to the ship crossing A2A: the first one occurs during P1L2 on day 60, the second one during P2L1 on day 100, and the third one during P2L2 on day 111 (see Figure 5). The peaks on day 72 during P1L2 and on day 115 during P2L2 occur when the ship crosses the warm tongue resulting from the complex interaction between A2, C4 and A1. The peak on day 125 during P2L2 occurs when the ship crosses the front where the cold tongue meets the southern warm water. Other sporadic mesoscale features occur during the simulated period, for example a small warm-core anticyclonic eddy located in the southeast corner of the area crossed by the ship on day 78 at the end of P1L2, and on days 84 and 91 during P2L1. The same reasoning applies to salinity, which is often associated with more prominent peaks than temperature (see Figure 8).

[51] Most of these features are well represented in the simulated fields, with the conclusion that the model is able to reproduce properly large-scale gradients in the area as well as mesoscale features (position and intensity) over the whole simulated period.

5.2. Vessel-Mounted Acoustic Doppler Current Profiler Data

[52] Time series of observed and simulated horizontal currents in the upper ocean along the ship track during P1L1, P1L2, P2L1 and P2L2 are shown in Figure 9. Horizontal current data are obtained from 15 min averaged *Atalante* VMADCP data in the 60–460 m layer. Simulated fields at data time in this layer are interpolated at data position. Semidiurnal oscillations are observed, particularly during the long CTD stations of P1L2 and P2L2. These

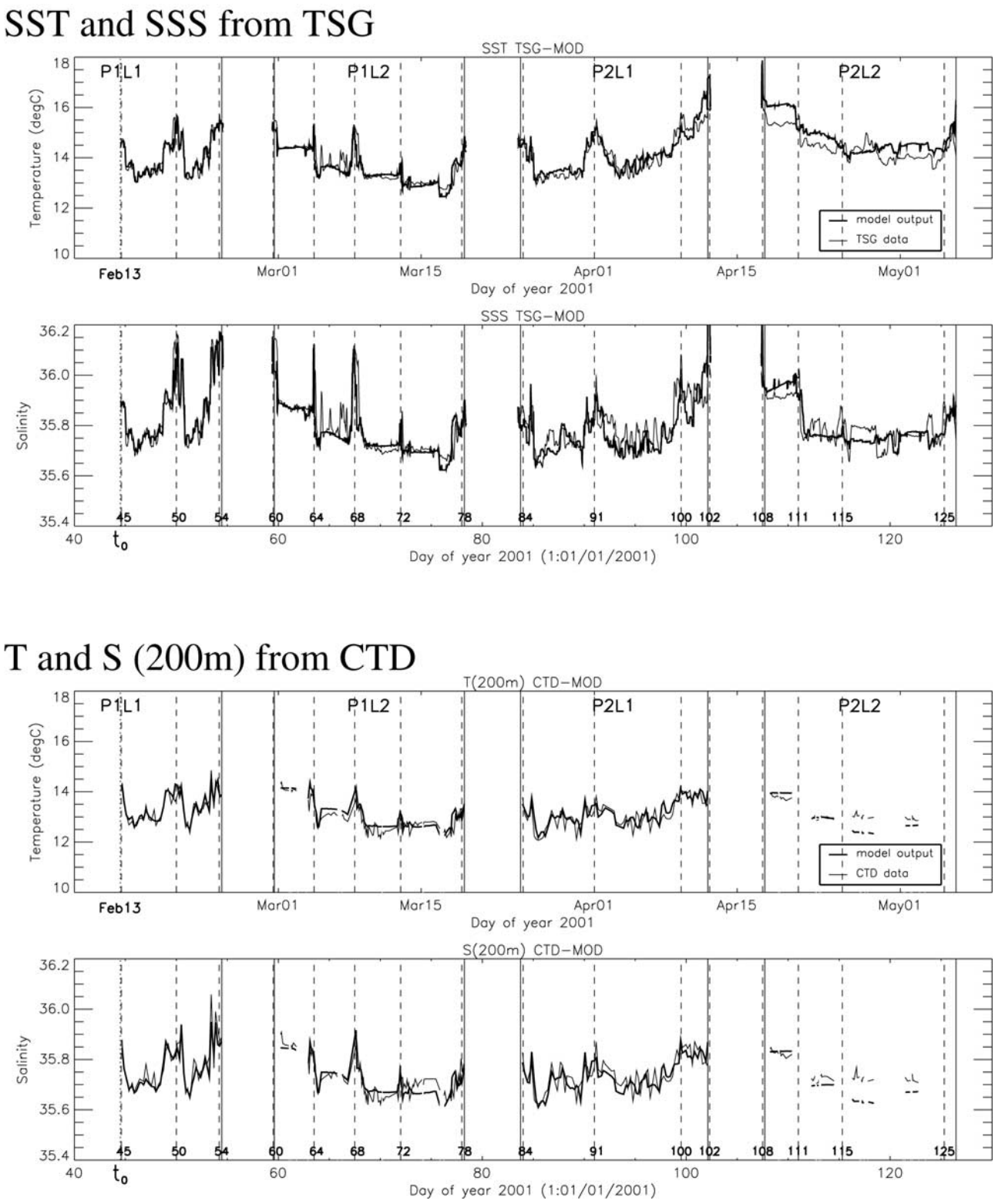

Figure 8. Surface and 200 m depth temperature and salinity from TSG and CTD during POMME 1 and POMME 2 following the ship track compared with model outputs.

oscillations are likely to be related to M2, the lunar semidiurnal ocean tide component of 12.4 hours period. Evidence of M2 was found by *Bouruet-Aubertot et al.* [2005] from the analysis of Eulerian measurements of horizontal currents collected over one year during the POMME experiment.

[53] As in the TSG and CTD data, many peaks that are indicative of mesoscale structures are present in the

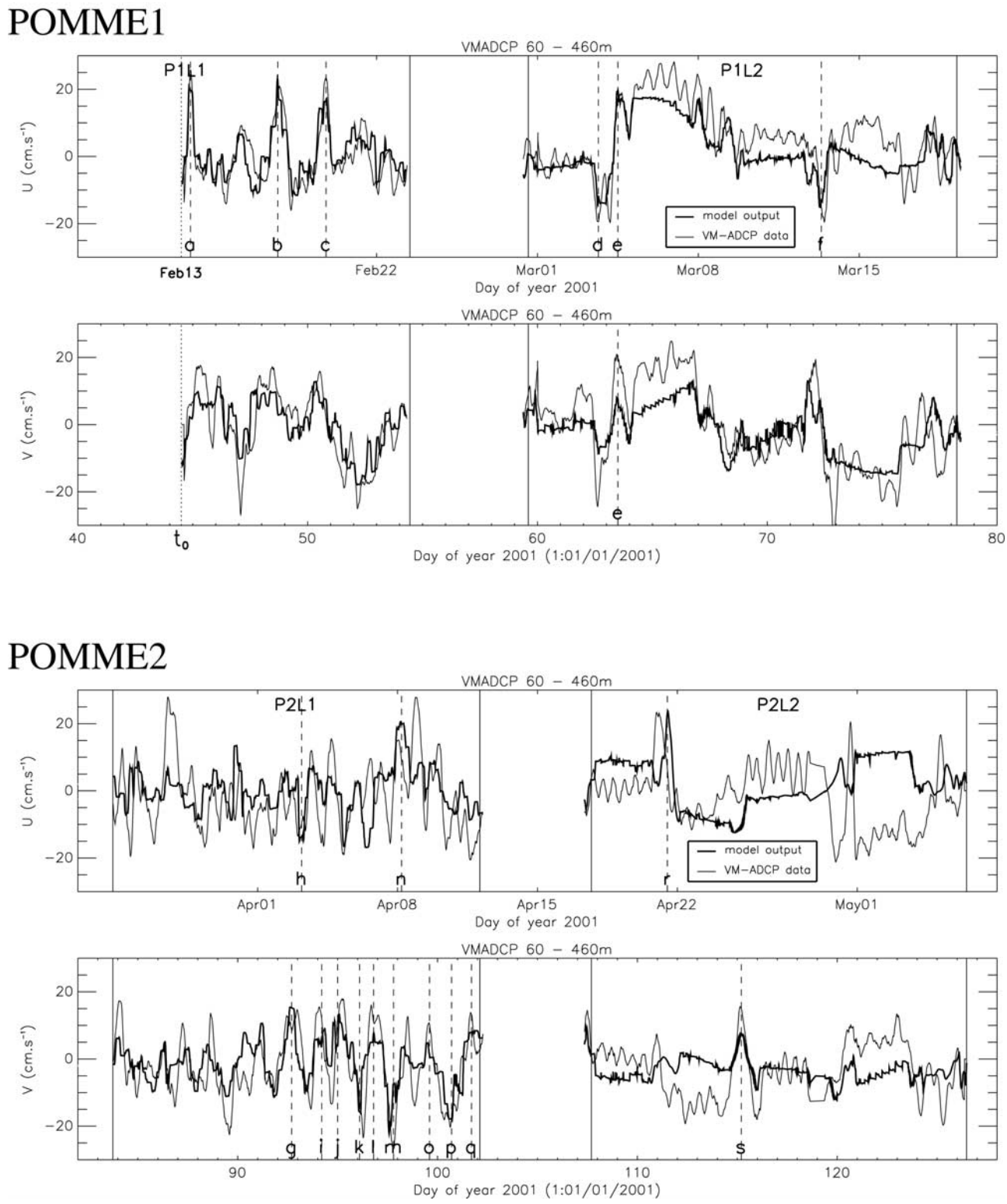

Figure 9. VMADCP velocities and model velocities during POMME 1 and POMME 2 following the ship track.

VMADCP data, and the most interesting of them are pointed out by vertical dashed lines in Figure 9. Ship positions corresponding to those peaks are indicated by white asterisks on the SLA fields in Figure 5. Each peak is identified by the same letter in Figure 5 and in Figure 9.

[54] During P1L1, three strong positive peaks (eastward currents) of about 20 cm s^{-1} are present in the zonal velocity (a, b and c in Figure 9). They are related to the front between A2 and C4, almost zonal during this period (see P1L1 snapshots in Figure 5). The agreement in location

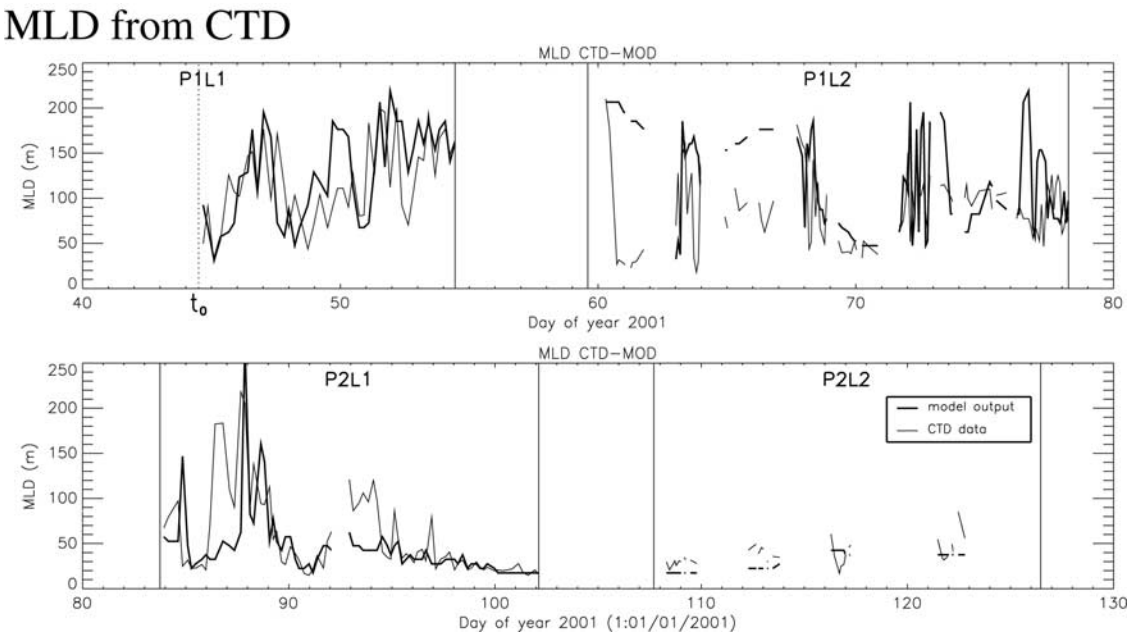

Figure 10. Mixed layer depth (MLD) computed from CTD data and from model output during POMME 1 and POMME 2 following the ship track.

and intensity between simulated and observed velocities during this period is excellent (the vectorial correlation coefficient is 0.80; see *Vialard* [1977] for details about calculation), as this period is the closest one to the initial state. This is a posteriori evidence of the initial state quality.

[55] During P1L2, the southwestward (peak d) and northeastward (peak e) currents, of about 17 cm s^{-1}, are associated with the anticyclonic eddy A2. The latter is interacting with a small anticyclonic eddy located around 41°N, 17.5°W to form these currents participating in the warm water northward motion and the cold water southward motion between P1 and P2 [*Mémery et al.*, 2005]. Peak f is associated with the northeastward current of about 20 cm s^{-1} at the perimeter of the anticyclonic eddy A1.

[56] P2L1 is probably the most interesting period for VMADCP currents. The anticyclonic eddy A1 has a signature in peaks i and j (10–15 cm s^{-1}). A1 entrains some cold water coming from the northeast corner, as attested by peak h (the southwestward current coming from this corner becomes almost zonal at about 15 cm s^{-1} on the southern side of A1). The cyclonic eddy C4 is obvious in peaks k and m, and also at the front between C4 and A2 in peaks m and n (about 20 cm s^{-1}). A2 is responsible for peaks p and q, while A2A is visible in peak o (about 5 cm s^{-1}). Peak g indicates warm water moving northward (at about 15 cm s^{-1}). During P2L2, the two peaks r and s, localized in the transition between stations, are associated with the cyclonic eddy C4 (note that there is a slight gap in the location of peak r between modeled and observed velocities).

[57] The agreement between the model and observed velocities is good, except during P2L2 for the reasons stated in section 5.1. If P2L2 is excluded, the vectorial correlation coefficient is 0.70, which is quite significant and is surprisingly high, as energy is largely in the mesoscale currents. It is important to point out that few numerical experiments are able to bear this kind of comparison. Except for some slight difference in location and for an underestimation (on average less than 20%), these mesoscale current peaks are well represented in the simulated fields. The conclusion is that the model is able to reproduce properly most of the mesoscale currents over the whole simulated period.

5.3. Mixed Layer Depth

[58] Time series of mixed layer depth computed using the same criterion (described in section 4.4) from CTD data and from simulated fields along the ship track during P1L1, P1L2, P2L1 and P2L2 are shown in Figure 10. This comparison is difficult because of the high temporal and spatial variability of the MLD fields, much larger than that of temperature, salinity and even horizontal currents fields, as shown in section 4.4. Moreover, the temporal frequency of the daily air-sea fluxes used may not be sufficient to reproduce the evolution of some in situ MLD conditions. Indeed, some diurnal variation of more than 100 m were observed between P1 and P2 on MLD computed from Carioca buoys [*Caniaux et al.*, 2004]. Work is in progress on a simulation using hourly air-sea fluxes. Advection of spatial variability may also play an important role in the evolution of the MLD.

[59] Nonetheless, even if the comparison between CTD- and model-computed MLD in Figure 10 shows that some MLD structures are missed by the simulation, the overall comparison is quite good. In particular, the variability is of the same order of magnitude in the CTD- and model-computed MLD, which is an important point indicating that the small MLD structures seen in Figure 6 are not likely to be numerical artifacts. Moreover, the domain-scale MLD south-north gradient is far from being as pronounced as in other coarser resolution studies in both CTD- and model-computed MLD (see Figure 11), supporting the results of section 4.4.

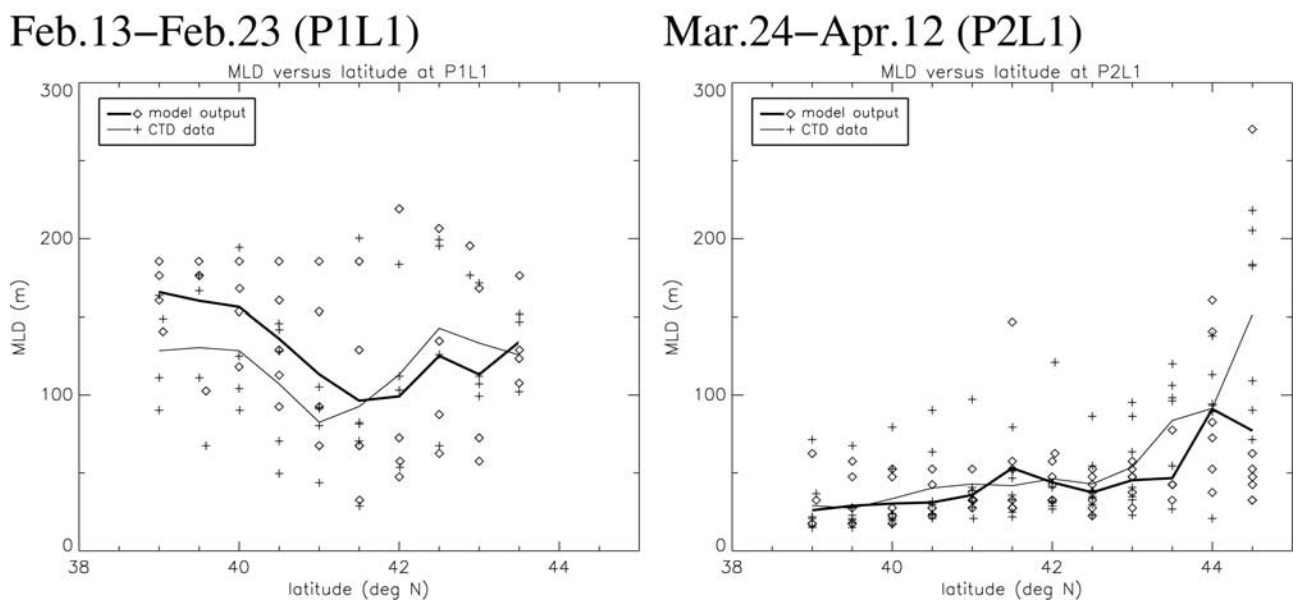

Figure 11. MLD computed from CTD data (crosses for value points and thin line for longitude-averaged values) and from model output (diamonds for value points and bold line for longitude-averaged values) as a function of latitude at P1L1 and P2L1. The domain-scale MLD south-north gradient is far from being as pronounced as in other coarser-resolution studies. Moreover, there is a high spatial variability linked to mesoscale structures. The comparison between longitude-averaged MLD computed from CTD data and from model output is good. The main discrepancy occurs at 44.5°N at P2L1. It is probably due to the proximity of the lateral boundaries that might perturb the simulation of some mesoscale structures, in particular A7.

5.4. Baroclinic Horizontal Mass Transports

[60] Up to now, only comparisons in the upper ocean have been presented. As the upper ocean dynamics depends on deeper adjustment and water masses, baroclinic horizontal transports by the geostrophic current will be presented, integrating not only upper ocean but also deeper water mass properties, such as North Atlantic Central Water (NACW), Mediterranean Water (MW) or North Atlantic Deep Water (NADW). Figure 12 shows SLA and these baroclinic transports for the 20–1670 m layer. Baroclinic transports are estimated from the P1L1 hydrological survey, and from the P2L1 hydrological survey and simulated fields at the same date. This calculation from in situ data is permitted owing to the sampling strategy using an even grid. Zonal and meridional baroclinic transports have been computed using the classical method described by *Fofonoff* [1962] for each box defined by four sampling points, and represented by a vector located at the box center. Note that the error on the densities deduced from CTD measurements leads to an uncertainty in the estimates of baroclinic transports in the 20–1670 m layer of about 0.4 Sv (1 Sv is 10^6 m^3 s^{-1}).

[61] During P2L1 (P2L1 data snapshot in Figure 12) the main frontal structure, located around 41°N between A2 and C4 and carrying about 6 Sv, develops two meridional meanders, transporting 3.3 Sv northward and 2.7 Sv southward, while this structure was almost zonal in the initial state (P1L1 data snapshot in Figure 12). The northward meander flows out between C4 and A1, and goes partly around A1 where it joins a southward current carrying cold water, the total resulting in a southward current transporting about 3.5 Sv of water. As demonstrated by a good vectorial correlation coefficient between P2L1 model in situ baroclinic transport anomalies (relative to P1L1 in situ baroclinic transports) and P2L1 in situ baroclinic transport anomalies, these main features are well reproduced in the simulated fields (P2L1 model snapshot in Figure 12). In fact, the coefficient value is 0.80, which is good for such a difficult comparison, integrating water properties over more than 1600 m, and taking into account water mass properties. The latter are therefore properly represented and located. Of course, locally there are some differences. For example, as shown by Table 1, baroclinic transport across the east and south boundaries are respectively underestimated and overestimated by the model. However model baroclinic transports across the west and north boundaries are satisfactory, as well as the resulting values for incoming (through north and south boundaries) and outgoing (through east and west boundaries) baroclinic transports. This points out that the recirculation area, which is a weakness for a limited area model, works well for this simulation. Note also that total baroclinic transport in the POMME domain deduced from in situ data vanishes, indicating that the temporal evolution of baroclinic transports was negligible over the survey duration at P2L1 (this was true at P1L1 as well).

6. Horizontal Scales Analysis: Mixed Layer and Vertical Velocities

[62] The model results show a large variety of horizontal scales of the order of 100 km in sea level anomalies (SLA) and temperature fields to the order of 10 km in mixed layer

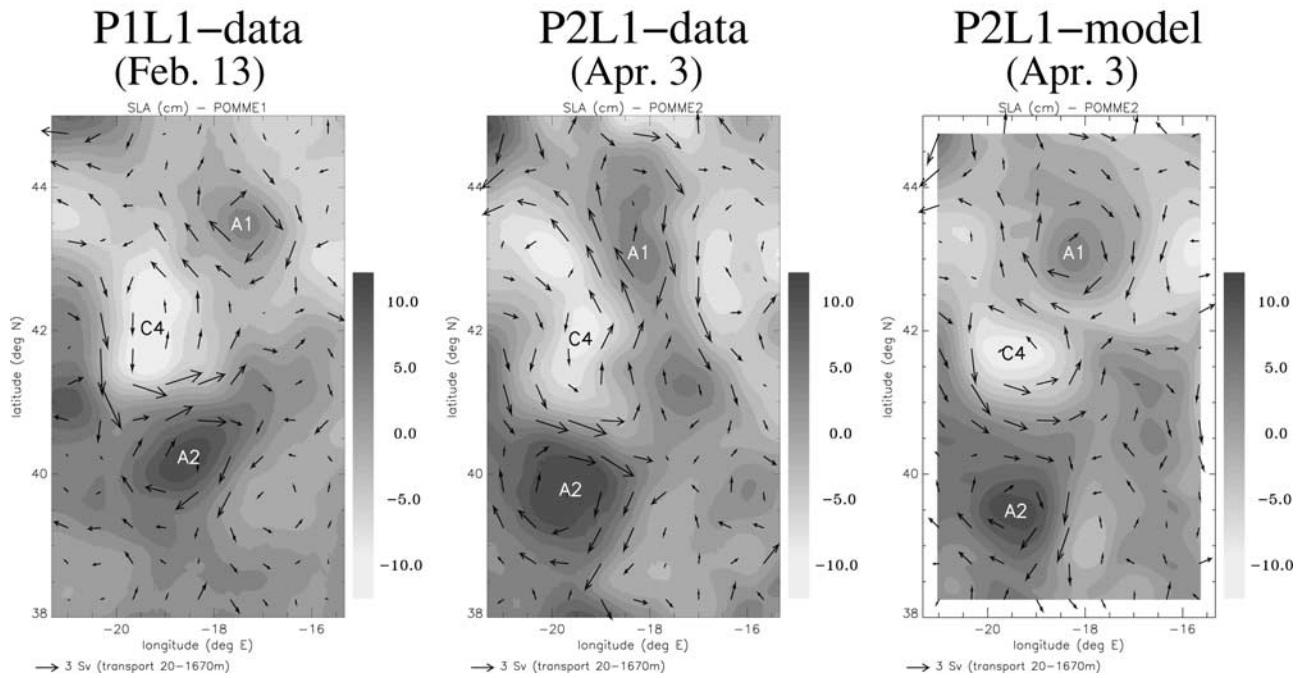

Figure 12. Sea level anomalies and baroclinic horizontal transports by the geostrophic current in the 20–1670 m layer estimated from P1L1 hydrological survey and from P2L1 hydrological survey and simulated fields at the same stage. The main mesoscale eddies, the frontal structure located around 41°N, and its northward meander are well reproduced by the model.

depth and vertical velocity fields (see Figure 6). In order to analyze these scales, two parameters are calculated in the POMME domain, excluding the model sponge layer. The first one is a length scale derived from autocorrelation functions. The second one is a slope calculated from variance spectra.

6.1. Autocorrelation Lengths

[63] A usual length scale derived from an autocorrelation function is its first zero crossing λ_0, but this scale may not be fully representative of the 2-D field considered. Indeed the first zero crossing is sensitive to the way the long wavelength signal (including the spatial averaging) is removed. Therefore a more robust length scale [*Le Traon et al.*, 1990; *Paillet*, 1999], defined as the integral of the autocorrelation function $C(r)$ from 0 to λ_0, is preferred here. $C(r)$ is calculated from a given simulated 2-D field X using the formula

$$C(r) = \frac{\mathrm{Cov}(r)}{\mathrm{Cov}(0)} \text{ where}$$

$$\begin{cases} \mathrm{Cov}(r) = \sum_{\vec{r},\ \|\vec{r}\| = r} \left(X(\vec{r}_l) - \overline{X}\right)\left(X(\vec{r}_l + \vec{r}) - \overline{X}\right) \\ \qquad\qquad \vec{r}_l,\ \vec{r}_l \in \text{2-D grid} \\ \overline{X} \text{ is the domain average of the 2-D field X} \\ r \text{ is a distance(the sum is done over annuli of radius } r) \end{cases} . \quad (4)$$

Then, λ_1 is defined as

$$\lambda_1 = \int_0^{\lambda_0} C(r)dr. \quad (5)$$

[64] Results for SLA, mixed layer depth and vertical velocity at 50 m depth are plotted as a function of time in Figure 13 (left-hand side). The SLA length scale is relatively constant at about 100 km, as expected for an ocean zone where mesoscale eddies are prevailing.

[65] The mixed layer length scale varies from 30 to 100 km, smaller values occurring during the shallowing period (day 60 to day 100, 1 March–10 April). As shown in Figure 6, the mixed layer shallowing does not occur at large scales, as expected, but at the submesoscale. Frontal structures between mesoscale eddies are obvious in the mixed layer depth field in Figure 6 and mesoscale eddies appear to be surrounded by mixed layer structures resulting from the interplay between mesoscale atmospheric forcing and the oceanic eddy vorticity field. At the beginning of the

Table 1. Baroclinic Transports Across Domain Border (Positive Values for Eastward and Northward Transports) and Mean Incoming and Outgoing Baroclinic Transports, Calculated From Simulated and In Situ Fields at P2L1[a]

Transport Across Border	Model Fields, Sv	In Situ Data, Sv
East	0.5	0.8
West	−5.7	−5.2
North	−5.3	−5.6
South	0.9	0.4
Mean Transport	**Model Fields, Sv**	**In Situ Data, Sv**
Outgoing (east and west)	6.2	6.0
Incoming (north and south)	6.2	6.0

[a]These baroclinic horizontal transports by the geostrophic current integrate water mass properties between 20 and 1670 m and provide an interesting validation of model outputs.

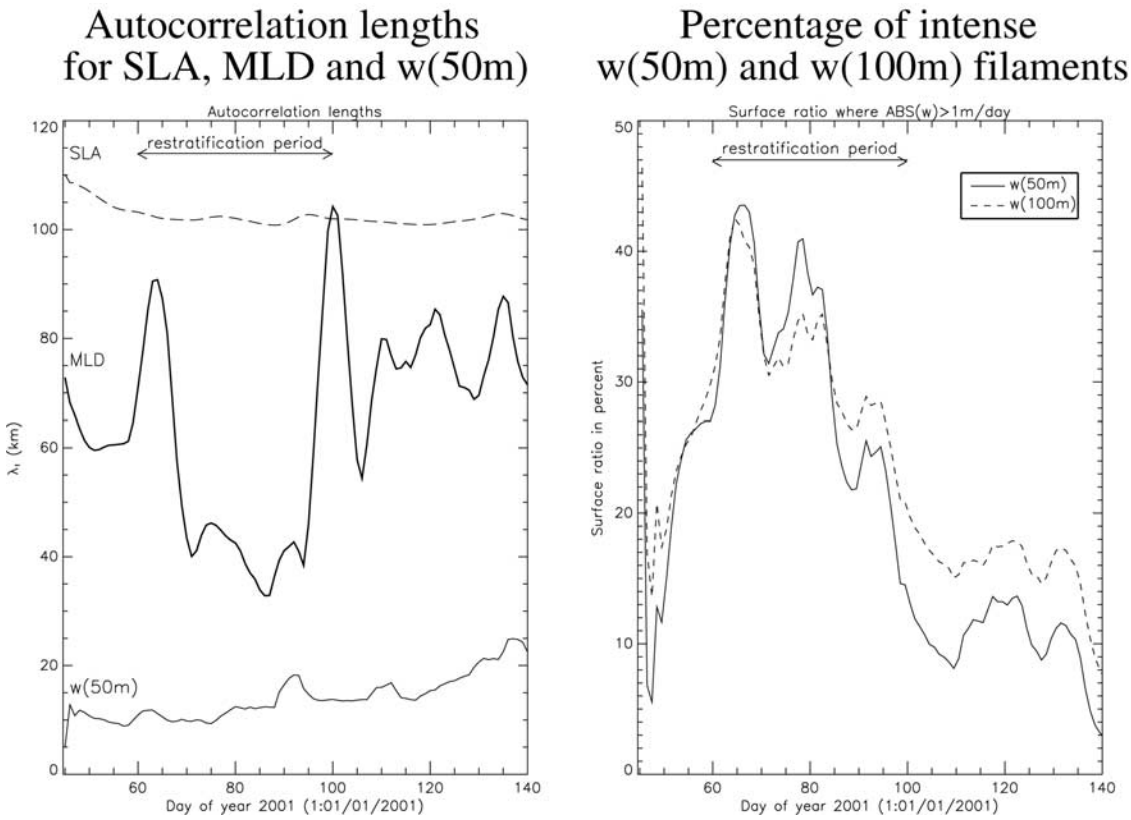

Figure 13. Temporal evolution of autocorrelation lengths for sea level anomalies (long-dashed line), mixed layer depth (bold line), and vertical velocity at 50 m depth (solid line), and temporal evolution of the percentage of intense vertical velocity filaments at 50 and 100 m. The mixed layer shallowing period (day 60 to day 100, 1 March–10 April) is associated with smaller mixed layer structures and intense vertical velocity submesoscale structures.

restratification period, the mixed layer shallowing occurs in a wide part of the southern part of the domain, and the MLD is quite uniform in this area, hence a peak of larger length scales around day 63. Then the shallowing occurs at the submesoscale, and the corresponding estimated length scale is about 40 km. After the restratification, the mixed layer is shallow in nearly all the domain, and the length scale is larger, about 80 km.

[66] Vertical velocity structures in the upper ocean are located at fronts between mesoscale eddies, as mixed layer structures. The correlation coefficient between the absolute value of vertical velocity and the relative vorticity gradient fields can reach 0.5, highest values being obtained when the restratification rate is at its maximum. These structures take the form of submesoscale filaments 10–20 km wide (see Figure 6). This length scale does not evolve much with time, as shown in Figure 13 (left-hand side), but there are more intense vertical velocity filaments during the restratification period in the upper ocean as shown in Figure 13 (right-hand side) for w at 50 m and 100 m depth. Results concerning the small-scale variability of w may be verified using RAFOS-VCM data, but the analysis of this data is still in progress. High-resolution color satellite images may also provide an indirect verification in terms of the small-scale variability of *w*, but this is not within the scope of this article.

[67] Note that the intensity of these structures may be underestimated due to their small size relative to the model resolution, but the overall shape is likely to be realistic. Indeed, very similar small-scale structures were observed in the same simulation but with a resolution of 2.5 km according to a test reported by *Lévy et al.* [2005] and in a different three dimensional numerical model simulation [*Giordani et al.*, 2005a, 2005b]. Even if these arguments do not come from observations, they provide evidence for the small-scale variability simulated and presented in this study.

6.2. Spectral Slopes

[68] Besides the typical scale present in a field (given by the autocorrelation length scale), it is also interesting to evaluate the relative importance of different scales. Therefore the spectral density of the variance, or variance spectrum, has been calculated for various dynamical quantities averaging the spectra deduced from a 1-D fast Fourier transform (FFT) applied to each north-south line of the model grid. This method has been used in preference to a 2-D fast Fourier transform applied directly to the 2-D field in order to compare model and data spectra. Indeed, it is more consistent to compare spectra calculated with the same method, and it is not possible to apply a 2-D FFT on data fields because high-resolution data are only available along

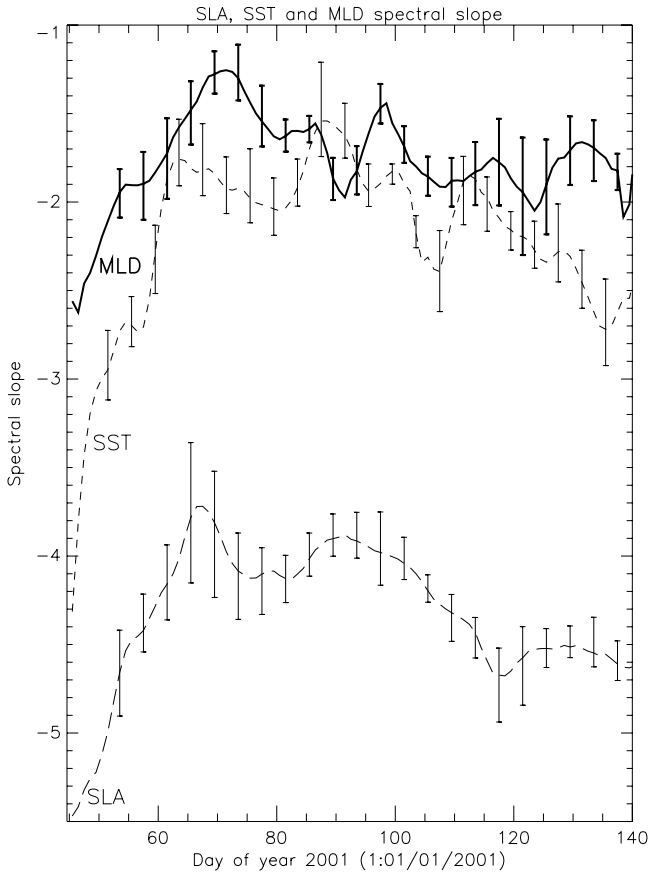

Figure 14. Temporal evolution of spectral slope between mesoscale and submesoscale structures for sea level anomalies (long-dashed line), sea surface temperature (short-dashed line), and mixed layer depth (bold line). Error bars have been evaluated by adding or subtracting one wavelength at each end of the interval used to calculate the spectral slope. The maximum and minimum values of the spectral slopes obtained provide an estimate for the error bars.

the ship tracks. Between a scale of 100–200 km and a scale of 10 km, these spectra are usually characterized by a power law of the form k^{-n} [*Lévy*, 2003; *Lévy and Klein*, 2004]. In order to compare the relative contribution to the total variance of mesoscale and submesoscale structures, the spectral slope $-n$ has been computed. Owing to numerical dissipation at the grid scale, the scaling behavior is not valid in the model fields for wavelengths as small as 10 km, but is for wavelengths as small as 30 km. The smaller n is, the more important the smaller-scale structures are relative to the mesoscale structures. The temporal evolution of this spectral slope for MLD, SST and SLA is given in Figure 14. Note that the results are very similar to those obtained from a 2-D FFT analysis carried out by *Lévy et al.* [2005].

[69] The initial fields used by the model are interpolated from a 25–50 km data analysis, and do not contain significant energy at the model grid scale (5 km). The model generates the missing scales, as shown by the increase in the slopes from the initial time, and the spectra are effectively spun up by approximately 10 days. This confirms what is seen, for example, in the simulated SST fields.

[70] The slope of SLA ($k^{-4.7}$ to $k^{-3.6}$) is consistent with the slopes observed in the North Atlantic by *Le Traon et al.* [1990], and with quasi-geostrophic turbulence theories that predict in the wave number domain of enstrophy cascade a k^{-3} slope for the velocity spectrum, equivalent through geostrophy to a k^{-5} slope for SLA [*Rhines*, 1979].

[71] The slope of simulated SST increases from day 45 to day 60, its maximum occurring during the restratification period (between day 60 and day 100), reaching $k^{-1.6}$. Then, the slope decreases to $k^{-2.7}$. This slope is consistent with the theoretical findings of *Klein et al.* [1998] (predicting k^{-2}), and with the slope calculated from TSG data, varying from $k^{-2.8}$ to $k^{-1.8}$ with a mean value of $k^{-2.4}$. These results may be also verified using high-resolution SST satellite data.

[72] The slope of the MLD spectrum is greater than the slope of the SST spectrum, indicating that submesoscale structures are more important in the MLD field than in the SST field relative to mesoscale structures. It is at its maximum around day 70, i.e., when the restratification rate is at its maximum, but it remains relatively high over the whole simulated period, except for the first 10 days. This shows that MLD submesoscale filaments are particularly present during the restratification period, as already shown in Figure 6 and section 6.1, but also that submesoscales remain important relative to the mesoscale over the period simulated. These results may be verified using high-resolution SeaSoar and Tow-Yo data, but the amount of data available is too small in time and space to have a representative estimate over the period simulated.

6.3. Horizontal Scales and Data Assimilation

[73] The regional model used has an altimetric sea level anomalies assimilation ability. The assimilation technique, described by *Gavart et al.* [1999], is based on locally lifting or lowering the water column and assuming no change in a reference pressure level.

[74] A sensitivity experiment using this ability has been conducted in order to quantify its impact on the model fields. Surprisingly enough, according to our comparison

Table 2. Correlation Between Model and Data Fields From P1L1 to P2L2 for the Run Presented in This Article and for the Same Run With Sea Level Anomaly (SLA) Assimilation[a]

Correlation Model/Data Fields	SST[b]	SSS[b]	T(200 m)[c]	S(200 m)[c]	(U, V)[d]	Transport[e]
Free run	0.92	0.87	0.89	0.88	0.70	0.80
SLA assimilation	0.89	0.81	0.75	0.68	0.59	0.71

[a]Results are not improved by the SLA assimilation.
[b]Sea surface temperature (SST) and sea surface salinity (SSS) from thermosalinograph.
[c]From conductivity-temperature-depth casts.
[d]Vessel-mounted acoustic Doppler current profiler horizontal currents in the 40–460 m layer.
[e]Baroclinic horizontal transport anomalies (relative to the P1L1 hydrological survey) in the 20–1670 m layer from the P2L1 hydrological survey.

with in situ data, the results are not improved and may even be slightly degraded (see Table 2). Similar results for biology are found by *Lévy et al.* [2005] in a coupled physics-biology simulation using the same model for physics, unlike what is usually found in studies using a lower-resolution model.

[75] These results underline the fact that our initial state, boundary conditions (including air-sea fluxes) and model are good enough not to be improved by the use of the satellite altimeter data assimilation method implemented in the model. However, simulation results were improved by this assimilation method applied to the same model but on a coarser grid and using data collected during the SEMAPHORE experiment [*Gavart et al.*, 1999]. Here the model resolution is such that the horizontal scales represented, on the order of 10 km, as shown in this section, are much smaller than assimilated scales from satellite altimetric sea level data. Therefore we suggest that, even if the assimilation method implemented in the model may improve results at the mesoscale, it may also produce artificial submesoscale structures resulting from the modification of the mesoscale structures which perturb the simulation. Indeed, no information at the submesoscale is provided by the assimilation. These perturbations deteriorate the simulation more than the assimilation improves it over the period of time simulated. This problem partly results from the adjustment of the system induced by the assimilation process. A solution is proposed by *Giordani et al.* [2005a, 2005b] through the use of a simplified three-dimensional model assimilating geostrophic currents. As a conclusion, particular attention needs to be paid to the initial state, assimilated data scales and assimilation method in order to produce realistic high-resolution simulations.

7. Conclusion

[76] A high-resolution simulation has been performed in order to integrate data isolated in time and space collected during the POMME experiments P1 and P2 into a realistic spatiotemporal representation of the upper ocean.

[77] Various validations show the very good quality of the simulation, and its ability to properly represent upper ocean temperature, salinity and circulation, as well as water mass properties in the POMME domain during the spring of 2001. The model performance and its resolution are such that the activation of the satellite altimetry assimilation method implemented here does not improve the results over the period of time simulated. This physical model has been coupled with a biological model by one of the authors and the resulting simulation has been validated for the biological fields [*Lévy et al.*, 2005], also providing an indirect and strong validation of the physical simulation. Note that these results indirectly validate the air-sea fluxes used to force the model [*Caniaux et al.*, 2005a, 2005b].

[78] The mixed layer shallowing, which is the oceanic response to air-sea flux warming, has been identified and described from the model simulation. It occurs from 1 March to 10 April of year 2001, and it is characterized by spatial and temporal heterogeneity. An horizontal scale analysis has shown that the MLD, vertical velocities, and SST contain significant submesoscale features that are filament-shaped located at fronts between mesoscale eddies. The smallest MLD structures and the most intense vertical velocity filaments have been observed during the restratification period.

[79] Finally, the quality of the simulation encourages its use to study physical processes in the upper ocean through upper ocean heat and salt budgets, and to describe the entrainment/detrainment field between P1 and P2, which is a key period for subduction. These points will be studied in a second paper (A. Paci et al., manuscript in preparation, 2005).

[80] **Acknowledgments.** The authors are grateful to the Hydrographic Service of the French Navy (SHOM) for the model high-resolution bathymetry, to the OPA system team for their development and maintenance of the LODYC ocean model, and to Youcef Amar for technical support. Comments and suggestions provided by Andreas Oschlies and two anonymous reviewers contributed to an improved presentation of these results. Thanks to Cyril Cichowlas for helpful discussions and to Anna Pirani for help in improving the English of this manuscript. The altimeter products were produced by the CLS Space Oceanography Division as part of the Environment and Climate EU ENACT project (EVK2-CT2001-00117) and with support from CNES. This study is a contribution to the POMME program managed by Laurent Mémery and Gilles Reverdin. Financial support was provided by the French research programs PATOM and PROOF and by the French agencies CNRS, IFREMER, Meteo-France, and SHOM. The data used results from a joint effort by all the POMME participants led by the onboard chief scientists Micheline Bianchi, Yves Desaubies, Jean-Claude Gascard, Fréderic Herpers, Patrick Mayzaud, Jérôme Paillet, and Louis Prieur.

References

Arakawa, A. (1972), Design of the UCLA general circulation model, *Rep. 7*, 116 pp., Dep. of Meteorol. Univ. of Calif., Los Angeles.

Arhan, M. (1990), The North Atlantic Current and Subarctic Intermediate Water, *J. Mar. Res.*, *48*, 109–144.

Assenbaum, M., and G. Reverdin (2005), Near real-time analyses of the mesoscale circulation during the POMME experiment, *Deep Sea Res., Part I*, in press.

Blanke, B., and P. Delecluse (1993), Variability of the tropical Atlantic Ocean simulated by a general circulation model with two different mixed-layer physics, *J. Phys. Oceanogr.*, *23*, 1363–1388.

Bougeault, P., and P. Lacarrère (1989), Parameterization of orography-induced turbulence in a mesobeta-scale model, *Mon. Weather Rev.*, *117*, 1872–1890.

Bourras, D., G. Reverdin, H. Giordani, and G. Caniaux (2004), Response of the atmospheric boundary layer to a mesoscale oceanic eddy in the northeast Atlantic, *J. Geophys. Res.*, *109*, D18114, doi:10.1029/2004JD004799.

Bouruet-Aubertot, P., H. Mercier, F. Gaillard, and P. Lherminier (2005), Evidence of strong inertia-gravity wave activity during the POMME experiment, *J. Geophys. Res.*, *110*, C07S06, doi:10.1029/2004JC002747.

Boyer, T. P., C. Stephens, J. I. Antonov, M. E. Conkright, R. A. Locarnini, T. D. O'Brien, and H. E. Garcia (2002), *World Ocean Atlas 2001*, vol. 2, *Salinity*, *NOAA Atlas NESDIS 49*, edited by S. Levitus, 167 pp., Natl. Oceanic and Atmos. Admin., Silver Spring, Md.

Brainerd, K. E., and M. C. Gregg (1995), Surface mixed and mixing layer depths, *Deep Sea Res., Part I*, *42*, 1521–1543.

Brisson, A., P. LeBorgne, A. Marsouin, and T. Moreau (1994), Surface irradiances calculated from Meteosat sensor data during SOFIA-ASTEX, *Int. J. Remote Sens.*, *1*, 197–203.

Caniaux, G., and S. Planton (1998), A three-dimensional ocean mesoscale simulation using data from the SEMAPHORE experiment: Mixed layer heat budget, *J. Geophys. Res.*, *103*, 25,081–25,099.

Caniaux, G., H. Roquet, and S. Planton (1993), A 3D mesoscale simulation of the ocean using data from the ATHENA88 field experiment, *J. Mar. Syst.*, *4*, 197–216.

Caniaux, G., L. Merlivat, L. Prieur, and H. Giordani (2004), Daily variation of oceanic mixed layers along drifter trajectories in the northeast Atlantic, *Geophys. Res. Abstr.*, *6*, abstract 03720.

Caniaux, G., A. Brut, D. Bourras, H. Giordani, A. Paci, L. Prieur, and G. Reverdin (2005a), A 1 year sea surface heat budget in the northeastern Atlantic basin during the POMME experiment: 1. Flux estimates, *J. Geophys. Res.*, *110*, C07S02, doi:10.1029/2004JC002596.

Caniaux, G., S. Belamari, H. Giordani, A. Paci, L. Prieur, and G. Reverdin (2005b), A 1 year sea surface heat budget in the northeastern Atlantic

basin during the POMME experiment: 2. Flux optimization, *J. Geophys. Res.*, *110*, C07803, doi:10.1029/2004JC002695.
Cresswell, G. R. (1982), The coalescence of two East Australian Current warm-core eddies, *Science*, *215*, 161–164.
Cresswell, G. R., and R. Legeckis (1986), Eddies off southeastern Australia, *Deep Sea Res., Part I*, *33*, 1527–1562.
de Boyer Montégut, C., G. Madec, A. S. Fischer, A. Lazar, and D. Iudicone (2004), Mixed layer depth over the global ocean: An examination of profile data and a profile-based climatology, *J. Geophys. Res.*, *109*, C12003, doi:10.1029/2004JC002378.
De Mey, P., and Y. Menard (1989), Synoptic analysis and dynamical adjustment of GEOS-3 and SEASAT altimeter eddy fields in the northwest Atlantic, *J. Geophys. Res.*, *94*, 6221–6230.
Dourado, M., and G. Caniaux (2001), Surface heat budget in an oceanic simulation using data from Tropical Ocean-Global Atmosphere Coupled Ocean-Atmosphere Response Experiment, *J. Geophys. Res.*, *106*, 16,623–16,640.
Eymard, L., et al. (1996), Study of the air-sea interactions at the mesoscale: The SEMAPHORE experiment, *Ann. Geophys.*, *14*, 986–1015.
Fofonoff, N. P. (1962), *The Sea: Ideas and Observations on Progress in the Study of the Seas*, vol. 1, *Physical Oceanography*, edited by M. N. Hill, pp. 323–395, Wiley Intersci., Hoboken, N. J.
Gaspar, P., Y. Grégoris, and J.-M. Lefèvre (1990), A simple eddy-kinetic-energy model for simulations of the oceanic vertical mixing: Tests at station Papa and Lotus site, *J. Geophys. Res.*, *95*, 16,179–16,193.
Gavart, M., P. De Mey, and G. Caniaux (1999), Assimilation of satellite altimeter data in a primitive-equation model of the Azores-Madeira region, *Dyn. Atmos. Oceans*, *29*, 217–254.
Giordani, H., G. Caniaux, and L. Prieur (2005a), A simplified 3D oceanic model assimilating geostrophic currents: Application to the POMME experiment, *J. Phys. Oceanogr.*, *35*, 628–644.
Giordani, H., G. Caniaux, L. Prieur, A. Paci, and S. Giraud (2005b), A 1 year mesoscale simulation in the northeast Atlantic: Mixed layer heat and detrainement-entrainment budgets during the POMME experiment, *J. Geophys. Res.*, *110*, C07S08, doi:10.1029/2004JC002765.
Griffiths, R. W., and E. J. Hopfinger (1987), Coalescing of geostrophic vortices, *J. Fluid Mech.*, *178*, 73–97.
Josse, P., G. Caniaux, H. Giordani, and S. Planton (1999), Intercomparison of oceanic and atmospheric forced and coupled mesoscale simulations, part 1: Surface fluxes, *Ann. Geophys.*, *17*, 566–576.
Klein, P., A. M. Treguier, and B. L. Hua (1998), Three-dimensional stirring of thermohaline fronts, *J. Mar. Res.*, *56*, 589–612.
Le Traon, P. Y., M. C. Rouquet, and C. Boissier (1990), Spatial scales of mesoscale variability in the North Atlantic as deduced from GEOSAT data, *J. Geophys. Res.*, *95*, 20,267–20,285.
Levitus, S., and T. P. Boyer (1994), *World Ocean Atlas 1994*, vol. 4, *Temperature*, *NOAA Atlas NESDIS 4*, 129 pp., Natl. Oceanic and Atmos. Admin., Silver Spring, Md.
Lévy, M. (2003), Mesoscale variability of phytoplankton and of new production: Impact of the large-scale nutrient distribution, *J. Geophys. Res.*, *108*(C11), 3358, doi:10.1029/2002JC001577.
Lévy, M., and P. Klein (2004), Does the low frequency variability of mesoscale dynamics explain a part of the phytoplankton and zooplankton spectral variability?, *Proc. R. Soc. London, Ser. A*, *460*, 1673–1687.
Lévy, M., P. Klein, and A. M. Treguier (2001), Impact of sub-mesoscale physics on production and subduction of phytoplankton in an oligotrophic regime, *J. Mar. Res.*, *59*, 535–565.
Lévy, M., M. Gavart, L. Mémery, G. Caniaux, and A. Paci (2005), A four-dimensional mesoscale map of the spring bloom in the northeast Atlantic (POMME experiment): Results of a prognostic model, *J. Geophys. Res.*, *110*, C07S21, doi:10.1029/2004JC002588.
Madec, G., P. Delecluse, M. Imbard, and C. Lévy (1999), OPA 8.1 Ocean General Circulation Model reference manual, *Note du Pôle de Modélisation du Climat 11*, Inst. Pierre-Simon Laplace, Paris.
Mahadevan, A., and D. Archer (1998), Modeling a limited region of the ocean, *J. Comput. Phys.*, *145*, 555–574.
Marshall, J. C., A. J. G. Nurser, and R. G. Williams (1993), Inferring the subduction rate and period over the North Atlantic, *J. Phys. Oceanogr.*, *23*, 1315–1329.
McCartney, M. S., and L. D. Talley (1982), The subpolar mode water of the North Atlantic Ocean, *J. Phys. Oceanogr.*, *12*, 1169–1188.
Mémery, L., G. Reverdin, J. Paillet, and A. Oschlies (2005), Introduction to the POMME special section: Thermocline ventilation and biogeochemical tracer distribution in the northeast Atlantic Ocean and impact of mesoscale dynamics, *J. Geophys. Res.*, *110*, C07S01, doi:10.1029/2005JC002976.
Mikhaylov, B. A., and V. M. Zolotarev (1970), Emissivity of liquid water, *Atmos. Oceanic Phys.*, *6*.
Paillet, J. (1999), Central water vortices of the eastern North Atlantic, *J. Phys. Oceanogr.*, *29*, 2487–2503.
Paillet, J., and M. Arhan (1996a), Shallow pycnoclines and mode water subduction in the eastern North Atlantic, *J. Phys. Oceanogr.*, *26*, 96–114.
Paillet, J., and M. Arhan (1996b), Oceanic ventilation in the eastern North Atlantic, *J. Phys. Oceanogr.*, *26*, 2036–2052.
Paillet, J., and H. Mercier (1997), An inverse model of the eastern North Atlantic general circulation and thermocline ventilation, *Deep Sea Res., Part I*, *44*, 1293–1328.
Payne, R. E. (1972), Albedo of the sea surface, *J. Atmos. Sci.*, *29*, 959–970.
Pollard, R. T., and L. A. Regier (1992), Vorticity and vertical circulation at an ocean front, *J. Phys. Oceanogr.*, *22*, 609–625.
Qiu, B., and R. X. Huang (1995), Ventilation of the North Atlantic and North Pacific: Subduction vs. obduction, *J. Phys. Oceanogr.*, *25*, 2374–2390.
Reverdin, G., M. Assenbaum, and L. Prieur (2005), Eastern North Atlantic Mode Waters during POMME (September 2000–2001), *J. Geophys. Res.*, *110*, C07S04, doi:10.1029/2004JC002613.
Rhines, P. B. (1979), Geostrophic turbulence, *Annu. Rev. Fluid Mech.*, *11*, 401–441.
Spall, M. A., R. A. Weller, and P. W. Furey (2000), Modeling the three-dimensional upper ocean heat budget and subduction rate during the Subduction Experiment, *J. Geophys. Res.*, *105*, 26,151–26,166.
Stephens, C., J. I. Antonov, T. P. Boyer, M. E. Conkright, R. A. Locarnini, T. D. O'Brien, and H. E. Garcia (2002), *World Ocean Atlas 2001*, vol. 1, *Temperature*, *NOAA Atlas NESDIS 49*, edited by S. Levitus, 167 pp., Natl. Oceanic and Atmos. Admin., Silver Spring, Md.
Stramma, L. (1984), Geostrophic transport in the warm water sphere of the eastern subtropical North Atlantic, *J. Mar. Res.*, *42*, 537–558.
Sundström, A., and T. Elvius (1979), *Computational Problems Related to Limited-Area Modeling*, *GARP Ser.*, no. 17, vol. 11, World Meteorol. Organ., Geneva, Switzerland.
Valdivieso da Costa, M., H. Mercier, and A. M. Tréguier (2005), Effect of the mixed-layer time variability on kinematic subduction rate diagnostics, *J. Phys. Oceanogr.*, *35*, 427–443.
Vialard, J. (1977), *Calcul des Probabilités et Statistique*, vol. 3, *Statistique Contingence et Corrélation*, Météo-France, Toulouse.
Weill, A., et al. (2003), Toward a better determination of turbulent air-sea fluxes from several experiments, *J. Clim.*, *16*, 600–618.
Weller, R. A., P. W. Furey, M. A. Spall, and R. E. Davis (2004), The large-scale context for oceanic subduction in the northeast Atlantic, *Deep Sea Res., Part I*, *51*, 665–699.
Williams, R. G., M. A. Spall, and J. C. Marshall (1995), Does Stommel's mixed layer "demon" work?, *J. Phys. Oceanogr.*, *25*, 3089–3102.

G. Caniaux, H. Giordani, and A. Paci, Météo-France/Centre National de Recherches Météorologiques–GAME, 42 avenue G. Coriolis, F-31057 Toulouse Cedex 01, France. (alexandre.paci@meteo.fr)

M. Gavart, Service Hydrologique et Océanographique de la Marine/Centre Militaire d'Océanographie/Recherche, Observatoire Midi-Pyrénées, 14 avenue E. Belin, F-31400 Toulouse, France.

M. Lévy and G. Reverdin, Laboratoire d'Océanographie Dynamique et de Climatologie/Institut Pierre-Simon Laplace, Université Paris VI, BP100, 4 place Jussieu, F-75252 Paris Cedex 05, France.

L. Prieur, Laboratoire d'Océanographie de Villefranche, BP 28, F-06234 Villefranche-sur-Mer Cedex, France.